

# Supporting Information

## Novel Strongly Correlated Europium Superhydrides

Dmitrii V. Semenov,<sup>1</sup> Di Zhou,<sup>2</sup> Alexander G. Kvashnin,<sup>1</sup> Xiaoli Huang,<sup>2,\*</sup> Michele Galasso,<sup>1</sup>  
Ivan A. Kruglov,<sup>3,4</sup> Anna G. Ivanova,<sup>5</sup> Alexander G. Gavriliuk,<sup>5,6</sup> Wuhao Chen,<sup>2</sup> Nikolay V. Tkachenko,<sup>7</sup>  
Alexander I. Boldyrev,<sup>7</sup> Ivan Troyan,<sup>5</sup> Artem R. Oganov,<sup>1,\*</sup> and Tian Cui<sup>8,2</sup>

<sup>1</sup> Skolkovo Institute of Science and Technology, Skolkovo Innovation Center, 3 Nobel Street, Moscow 143026, Russia

<sup>2</sup> State Key Laboratory of Superhard Materials, College of Physics, Jilin University, Changchun 130012, China

<sup>3</sup> Moscow Institute of Physics and Technology, 9 Institutsky Lane, Dolgoprudny 141700, Russia

<sup>4</sup> Dukhov Research Institute of Automatics (VNIIA), Moscow 127055, Russia

<sup>5</sup> Shubnikov Institute of Crystallography, Federal Scientific Research Center Crystallography and Photonics, Russian Academy of Sciences, 59 Leninskii pr-t, Moscow 119333, Russia

<sup>6</sup> IC RAS Institute for Nuclear Research, Russian Academy of Sciences, Moscow 117312, Russia

<sup>7</sup> Department of Chemistry and Biochemistry, Utah State University, 0300 Old Main Hill, Logan, Utah, 84322-0300, USA

<sup>8</sup> School of Physical Science and Technology, Ningbo University, Ningbo 315211, China

### Corresponding Authors

Dr. X. Huang, e-mail: huangxiaoli@jlu.edu.cn, Prof. A. Oganov, e-mail: a.oganov@skoltech.ru

### Contents

|   |     |
|---|-----|
| Methods.....                                | S2  |
| <i>Experiment</i> .....                     | S2  |
| <i>Theory</i> .....                         | S2  |
| Structural Information.....                 | S4  |
| Additional Le Bail Refinements .....        | S14 |
| Magnetic Structure.....                     | S16 |
| Natural Population Analysis .....           | S23 |
| Electronic Band Structure .....             | S25 |
| Phonon Spectra .....                        | S28 |
| Anharmonic Calculations.....                | S30 |
| Elastic Properties of the Eu–H Phases ..... | S32 |
| References.....                             | S32 |

## Methods

### Experiment

To investigate the formation of new chemical compounds in the Eu–H system, we purchased the europium foil with 99.99% purity from Alfa Aesar company. Two diamond anvil cells (DACs) with 100 and 150  $\mu\text{m}$  culets were loaded with Eu and ammonia borane (AB), purified by sublimation, which was used as a source of hydrogen and a pressure transmitting medium (Table S1). As has been shown earlier in the synthesis of superhydrides of lanthanum,<sup>1</sup> thorium,<sup>2</sup> praseodymium,<sup>3</sup> and neodymium,<sup>4</sup> ammonia borane is an effective source of hydrogen when the metal target is heated by a short ( $< 0.2$  s) laser pulse due to the well-known thermal decomposition reaction:  $\text{NH}_3\text{BH}_3 \rightarrow \text{H}_2 + \text{poly}(\text{BNH}_x)_n$ .<sup>5,6</sup>

A tungsten plate with a thickness of  $20 \pm 2$   $\mu\text{m}$  was used as a gasket. The pressure was determined by the Raman signal of diamond.<sup>7</sup> Heating was carried out by pulses of an infrared laser (1  $\mu\text{m}$ , Nd:YAG). A part of the X-ray diffraction (XRD) patterns of all samples studied in diamond anvil cells were recorded on 4W2 beamline of the Beijing Synchrotron Research Facilities (BSRF, China) and BL15U1 synchrotron beamline at the Shanghai Synchrotron Research Facility (SSRF, China)<sup>8</sup> using a focused ( $5 \times 12$   $\mu\text{m}$ ) monochromatic X-ray beam (20 keV, 0.6199  $\text{\AA}$ ). The other part of the high-pressure XRD patterns were obtained at BL10XU in SPring-8 using monochromatic synchrotron radiation and an imaging plate detector at room temperature.<sup>9</sup> The X-ray beam with a wavelength of 0.413  $\text{\AA}$  was focused with a polymer compound refractive lens (SU-8, produced by ANKA). The experimental X-ray diffraction images were analyzed and integrated using Dioptas software package.<sup>10</sup> The full profile analysis of the diffraction patterns and calculations of the unit cell parameters were performed in JANA2006<sup>11</sup> using the Le Bail method.<sup>12</sup> Additional parameters of high-pressure diamond anvil cells are listed in Table S1.

**Table S1.** Experimental parameters of the DACs used to synthesize europium hydrides.

| Cell | Synthesis pressure, GPa | Culet size, $\mu\text{m}$ | Sample size, $\mu\text{m}$ | Composition/load                   |
|------|-------------------------|---------------------------|----------------------------|------------------------------------|
| E1   | 110                     | 100                       | 15                         | Eu/BH <sub>3</sub> NH <sub>3</sub> |
| E2   | 74                      | 150                       | 20                         | Eu/BH <sub>3</sub> NH <sub>3</sub> |
| E3   | 86                      | 100                       | 13                         | Eu/BH <sub>3</sub> NH <sub>3</sub> |

### Theory

All calculations of crystalline systems were carried out using the Vienna Ab initio Simulation Package (VASP) code<sup>13–15</sup> with PAW<sup>16–18</sup> pseudopotentials. The calculations were performed solely for producing the wave functions of the systems. The generalized gradient approximation (GGA) expressed by the PBE functional was applied. The Brillouin zone was sampled using the Monkhorst–Pack method.<sup>19</sup> Considering the different number of atoms in unit cells for different compounds, various  $k$ -grids ( $5 \times 5 \times 5$  and  $11 \times 11 \times 11$ ) were used. The energy cutoff was set to 600 eV, the partial occupancies were set using the Gaussian smearing with  $\sigma = 0.1$ . To find the bonding pattern of the selected clusters, the solid-state adaptive natural density partitioning (SSAdNDP)<sup>20</sup> algorithm was implemented. The SSAdNDP follows the idea of the AdNDP algorithm for molecules<sup>21,22</sup> and the periodic NBO method.<sup>23</sup> It is based on the partitioning of the electron density (1-body density matrix) and produces the interpretation of chemical bonding in systems with translational symmetry in terms of classical lone pairs and two-center bonds, as well as multicenter delocalized bonding. The algorithm produces the number of bonding elements and their occupancy numbers (ONs). Physically, it shows how many electrons are sitting in the chosen region. For the ideal Lewis case, the ON is  $2.00 |e|$ . It has been shown that the chemical bonding pattern obtained with the SSAdNDP has a high correlation with features of studied materials and can give important insights into the physical and chemical properties of various solids.<sup>24–28</sup> The Stuttgart RSC 1997 ECP atomic

centered basis<sup>29</sup> for actinides and Def2-TZVPP<sup>30</sup> basis for other atoms were used to represent the projected PW density. For convenience, we designate this basis set combination as Basis\_1. The spillage parameter of occupied bands for this basis was no higher than 1%. For spin-polarized calculations, both spin-up (alpha) and spin-down (beta) density matrices were analyzed. The resulting bonding elements were designated as alpha and beta bonds. The occupancies of doubly occupied bonding elements for spin-polarized cases were calculated as a sum of the occupancies of alpha and beta bonding elements.

For calculations of the model clusters, the Gaussian 16 program<sup>31</sup> was used. The exact geometries of the solid-state hydrides were taken for modeling the wave functions. The charges of clusters were set so as to take into account the stoichiometry of the crystals. All calculations were carried out at the PBE0/Basis\_1 level of theory. The ChemCraft 1.8 software<sup>32</sup> was used to visualize the chemical bonding patterns and geometries of the investigated hydrides.

The calculations of the electron–phonon coupling and superconducting  $T_C$  were carried out with QUANTUM ESPRESSO (QE) package<sup>32</sup> using the density functional perturbation theory,<sup>33</sup> employing the plane-wave generalized gradient approximation with the Goedecker–Hartwigsen–Hutter–Teter pseudopotentials.<sup>34,35</sup> In our ab initio calculations of the electron–phonon coupling (EPC) parameter  $\lambda$  of EuH<sub>9</sub>, the first Brillouin zone was sampled by  $2 \times 2 \times 2$   $q$ -points mesh and  $10 \times 10 \times 10$   $k$ -points meshes with a smearing  $\sigma = 0.005$ – $0.05$  Ry that approximates the zero-width limits in the calculation of  $\lambda$ . The critical temperature  $T_C$  was calculated using the Allen–Dynes equations.<sup>36</sup>

To calculate  $U$ – $J$ , we took the most stable collinear states for each of the three phases (AFM  $2F\bar{4}3m$ -EuH<sub>9</sub>, FM  $P6_3/mmc$ -EuH<sub>9</sub>, and FM  $Pm\bar{3}n$ -Eu<sub>8</sub>H<sub>46</sub>) and the computed DFT ground state with  $U$ – $J = 0$ . Then, we computed the “bare” and “interacting” responses by applying a series of small perturbations ( $\alpha = -0.08, -0.05, -0.02, 0.02, 0.05, 0.08$ ) to one of the Eu sites. We obtained the response functions from a linear fit of the number of  $f$  electrons on the perturbed atomic site as a function of the applied potential  $\alpha$  (Figure S4). From the slopes of these functions we obtained the value of  $U$ – $J$  (Table S6). The obtained results were close to those previously described in the study of  $P6_3/mmc$ -NdH<sub>9</sub>.<sup>4</sup>

Before starting the magnetic calculations, we checked the parameters for convergence. After several tests with different VASP pseudopotentials (Eu\_2, Eu), we noticed that the computed magnetization on each atom was always zero, which is physically meaningless. The only pseudopotential which allowed us to study the magnetic properties of EuH<sub>9</sub> is Eu (PAW\_PBE\_Eu\_23Dec2003,  $z_{\text{val}} = 17$ ), so we used it together with that of H, both taken from the VASP library. The kinetic energy cutoff of the plane wave basis set was chosen to be 540 eV (520 eV) for the  $F\bar{4}3m$  ( $P6_3/mmc$ ) phase, which gives a maximum error of 1 meV/atom with respect to more accurate calculations. The same error criterion was used when choosing, for both EuH<sub>9</sub> phases, a length  $l = 40$  for the automatic generation of GAMMA-centered Monkhorst–Pack grids as implemented in the VASP code, and a smearing parameter SIGMA = 0.2 with the Methfessel–Paxton method of order 1.

## Structural Information

Table S2. Calculated (SOC, DFT+U,  $U-J = 5$  eV) crystal structure of the discovered Eu–H phases.

| Phase   | Pressure, | Lattice  | Coordinates |          |          |          |
|---|-----------|--|-------------|----------|----------|----------|
| $P6_3/mmc$ -EuH <sub>9</sub>                  | 100       | $a = 3.559 \text{ \AA}$<br>$c = 5.855 \text{ \AA}$<br>$\alpha = \beta = \gamma = 90^\circ$   | Eu1         | 0.33333  | 0.66667  | 0.75000  |
|   |           |  | H1          | 0.00000  | 0.00000  | 0.25000  |
|   |           |  | H2          | 0.33333  | 0.66667  | 0.33627  |
|   |           |  | H3          | 0.15200  | 0.30401  | 0.04717  |
| $F\bar{4}3m$ -EuH <sub>9</sub>                | 100       | $a = 5.041 \text{ \AA}$<br>$\alpha = \beta = \gamma = 90^\circ$  | Eu1         | 0.25000  | 0.25000  | 0.25000  |
|   |           |  | H1          | -0.13655 | -0.13655 | -0.13655 |
|   |           |  | H2          | -0.38097 | -0.38097 | -0.38097 |
|   |           |  | H3          | 0.00000  | 0.00000  | 0.00000  |
| $Pm\bar{3}n$ -Eu <sub>4</sub> H <sub>46</sub> | 130       | $a = 5.865 \text{ \AA}$<br>$\alpha = \beta = \gamma = 90^\circ$  | Eu1         | 0.00000  | 0.00000  | 0.00000  |
|   |           |  | Eu2         | 0.25000  | 0.00000  | 0.50000  |
|   |           |  | H1          | 0.00000  | 0.11963  | 0.30584  |
|   |           |  | H2          | 0.25000  | 0.50000  | 0.00000  |
|   |           |  | H3          | 0.18451  | 0.18451  | 0.18451  |
| $Fm\bar{3}n$ -EuH <sub>10</sub>               | 100       | $a = 5.183 \text{ \AA}$<br>$\alpha = \beta = \gamma = 90^\circ$  | Eu          | 0.00000  | 0.00000  | 0.00000  |
|   |           |  | H1          | 0.11916  | 0.11916  | 0.11916  |
|   |           |  | H2          | 0.25000  | 0.25000  | 0.25000  |
| $P1$ -EuH <sub>9</sub><br>(pseudo-hexagonal)  | 130       | $a=3.5598 \text{ \AA}$<br>$b=6.8524 \text{ \AA}$<br>$c=6.1657 \text{ \AA}$<br>$\alpha=63.26^\circ$<br>$\beta=90^\circ$<br>$\gamma=74.94^\circ$ | Eu1         | 0.375    | 0.25     | 0.708333 |
|   |           |  | Eu2         | 0.625    | 0.75     | 0.291667 |
|   |           |  | Eu3         | 0.875    | 0.25     | 0.208333 |
|   |           |  | Eu4         | 0.125    | 0.75     | 0.791667 |
|   |           |  | H1          | 0.625    | 0.75     | 0.625    |
|   |           |  | H2          | 0.125    | 0.75     | 0.125    |
|   |           |  | H3          | 0.875    | 0.25     | 0.875    |
|   |           |  | H4          | 0.375    | 0.25     | 0.375    |
|   |           |  | H5          | 0.918135 | 0.16373  | 0.584801 |
|   |           |  | H6          | 0.418135 | 0.16373  | 0.084801 |
|   |           |  | H7          | 0.081865 | 0.83627  | 0.415199 |
|   |           |  | H8          | 0.581865 | 0.83627  | 0.915199 |
|   |           |  | H9          | 0.168135 | 0.66373  | 0.501468 |
|   |           |  | H10         | 0.668135 | 0.66373  | 0.001468 |
|   |           |  | H11         | 0.831865 | 0.33627  | 0.498532 |
|   |           |  | H12         | 0.331865 | 0.33627  | 0.998532 |
|   |           |  | H13         | 0.501592 | 0.452831 | 0.349587 |
|   |           |  | H14         | 0.001592 | 0.452831 | 0.849587 |
|   |           |  | H15         | 0.498408 | 0.547169 | 0.650413 |
|   |           |  | H16         | 0.998408 | 0.547169 | 0.150413 |
|   |           |  | H17         | 0.773584 | 0.452831 | 0.621579 |
|   |           |  | H18         | 0.273584 | 0.452831 | 0.121579 |
|   |           |  | H19         | 0.226416 | 0.547169 | 0.378421 |
| H20   | 0.726416  | 0.547169   | 0.878421    |          |          |          |
| H21   | 0.045577  | 0.452831   | 0.349587    |          |          |          |
| H22   | 0.545577  | 0.452831   | 0.849587    |          |          |          |
| H23   | 0.954423  | 0.547169   | 0.650413    |          |          |          |

|  |     |   |     |          |          |          |
|--|-----|---|-----|----------|----------|----------|
|  |     |   | H24 | 0.454423 | 0.547169 | 0.150413 |
|  |     |   | H25 | 0.295577 | 0.952831 | 0.447582 |
|  |     |   | H26 | 0.795577 | 0.952831 | 0.947582 |
|  |     |   | H27 | 0.704423 | 0.047169 | 0.552418 |
|  |     |   | H28 | 0.204423 | 0.047169 | 0.052418 |
|  |     |   | H29 | 0.023584 | 0.952831 | 0.175589 |
|  |     |   | H30 | 0.523584 | 0.952831 | 0.675589 |
|  |     |   | H31 | 0.976416 | 0.047169 | 0.82441  |
|  |     |   | H32 | 0.476416 | 0.047169 | 0.32441  |
|  |     |   | H33 | 0.751592 | 0.952831 | 0.447582 |
|  |     |   | H34 | 0.251592 | 0.952831 | 0.947582 |
|  |     |   | H35 | 0.248408 | 0.047169 | 0.552418 |
|  |     |   | H36 | 0.748408 | 0.047169 | 0.052418 |
| <i>P1</i> -EuH <sub>9</sub><br>(pseudocubic) | 130 | $a=3.5646 \text{ \AA}$<br>$b=3.5646 \text{ \AA}$<br>$c=6.1742 \text{ \AA}$<br>$\alpha=90^\circ$<br>$\beta=73.22^\circ$<br>$\gamma=60^\circ$ | Eu1 | 0.75     | 0.125    | 0.375    |
|  |     |   | Eu2 | 0.75     | 0.625    | 0.875    |
|  |     |   | H1  | 0.59035  | 0.204825 | 0.068275 |
|  |     |   | H2  | 0.59035  | 0.704825 | 0.568275 |
|  |     |   | H3  | 0.13655  | 0.658625 | 0.068275 |
|  |     |   | H4  | 0.13655  | 0.158625 | 0.568275 |
|  |     |   | H5  | 0.13655  | 0.431725 | 0.295175 |
|  |     |   | H6  | 0.13655  | 0.931725 | 0.795175 |
|  |     |   | H7  | 0.13655  | 0.204825 | 0.068275 |
|  |     |   | H8  | 0.13655  | 0.704825 | 0.568275 |
|  |     |   | H9  | 0.857095 | 0.571452 | 0.190484 |
|  |     |   | H10 | 0.857095 | 0.071452 | 0.690484 |
|  |     |   | H11 | 0.380968 | 0.047579 | 0.190484 |
|  |     |   | H12 | 0.380968 | 0.547579 | 0.690484 |
|  |     |   | H13 | 0.380968 | 0.809515 | 0.428548 |
|  |     |   | H14 | 0.380968 | 0.309515 | 0.928548 |
|  |     |   | H15 | 0.380968 | 0.571452 | 0.190484 |
|  |     |   | H16 | 0.380968 | 0.071452 | 0.690484 |
| H17  | 0.0 | 0.0   | 0.0 |          |          |          |
| H18  | 0.0 | 0.5   | 0.5 |          |          |          |

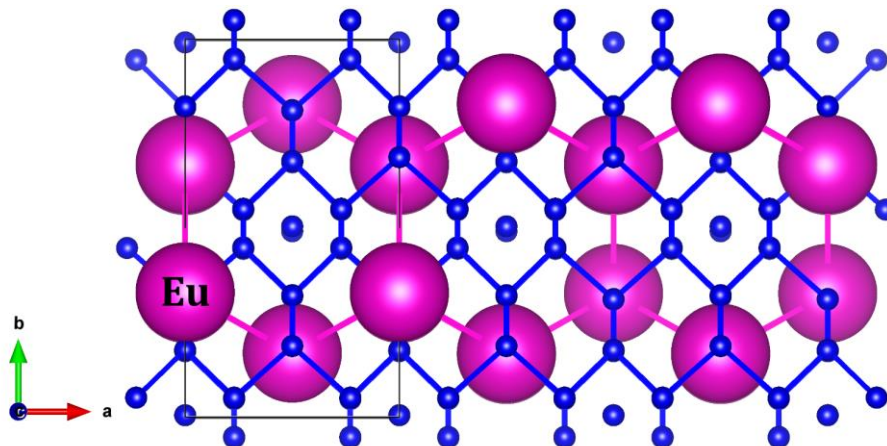


**Figure S1.** Crystal structure of pseudo-hexagonal *P1*(hex)-EuH<sub>9</sub> (=Eu<sub>4</sub>H<sub>36</sub>) with the disordered hydrogen sublattice, visualized using VESTA software.<sup>37</sup> The hydrogen atoms are shown in blue.

**Table S3.** Experimental and theoretical cell parameters of all studied Eu–H phases.  $V_{\text{DFT+U}}$  is calculated with SOC and  $U-J = 5$  eV,  $V_{\text{DFT}}$  is calculated without the Hubbard correction. Data in brackets correspond to experiment at  $\lambda = 0.6199$  Å and  $0.413$  Å.

| Compound   | Pressure, GPa | $a$ , Å            | $c$ , Å            | $V$ , Å <sup>3</sup><br>per Eu atom | $V_{\text{DFT+U}}$ , Å <sup>3</sup><br>per Eu atom | $V_{\text{DFT}}$ , Å <sup>3</sup><br>per Eu atom |
|--|---------------|--------------------|--------------------|-------------------------------------|--|--|
| $Pm\bar{3}n$ -Eu <sub>8</sub> H <sub>46</sub><br>( $Z = 8$ ) | 130           | 5.8582             |                    | 25.13                               | 25.21  | 24.75  |
|  | 125           | 5.8604             |                    | 25.16                               | 25.49  | 25.02  |
|  | 121           | 5.8649             |                    | 25.22                               | 25.77  | 25.29  |
|  | 116           | 5.8862             |                    | 25.49                               | 26.08  | 25.58  |
|  | 111           | 5.9069<br>(5.9080) |                    | 25.76<br>(25.77)                    | 26.38  | 25.88  |
|  | 106           | 5.9492             |                    | 26.32                               | 26.65  | 26.15  |
|  | 102           | 5.9547             |                    | 26.39                               | 26.92  | 26.38  |
|  | 99            | 5.9656             |                    | 26.54                               | 27.13  | 26.58  |
|  | 97            | 5.9729             |                    | 26.63                               | 27.26  | 26.71  |
|  | 94            | 5.9732             |                    | 26.64                               | 27.54  | 26.96  |
|  | 90            | 5.9839             |                    | 26.78                               | 27.79  | 27.21  |
|  | 89            | 6.0125             |                    | 27.17                               | 27.80  | 26.87  |
|  | 86            | 5.9973             |                    | 26.96                               | 28.12  | 27.51  |
| $P6_3/mmc$ -EuH <sub>9</sub><br>( $Z = 2$ )                  | 130           | 3.5911<br>(3.5887) | 5.5094<br>(5.5027) | 30.76<br>(30.68)                    | 30.01  | 29.34  |
|  | 125           | 3.5870             | 5.5176             | 30.74                               | 31.38  | 30.53  |
|  | 121           | 3.5905             | 5.5265             | 30.85                               | 31.67  | 30.85  |
|  | 118           | 3.5992             | 5.5419             | (31.085)                            | 31.89  | 31.00  |
|  | 116           | 3.5914             | 5.6063             | 31.31                               | 32.07  | 31.19  |
|  | 111           | 3.6203             | 5.5171             | 31.31                               | 32.51  | 31.62  |
| $F\bar{4}3m$ -EuH <sub>9</sub><br>( $Z = 4$ )                | 130           | 4.9475             |                    | 30.27                               | 30.67  | 29.92  |
|  | 125           | 4.9472             |                    | 30.27                               | 30.98  | 30.28  |
|  | 121           | 4.9566             |                    | 30.44                               | 31.26  | 30.57  |
|  | 116           | 4.9741             |                    | 30.77                               | 31.63  | 30.90  |
|  | 111           | 4.9786             |                    | 30.85                               | 32.04  | 31.33  |
|  | 106           | 5.0313             |                    | 31.84                               | 32.43  | 31.67  |
|  | 102           | 5.0439             |                    | 32.08                               | 32.76  | 32.00  |
|  | 99            | 5.0589             |                    | 32.37                               | 33.01  | 32.23  |
|  | 97            | 5.0700             |                    | 32.58                               | 33.20  | 32.42  |
|  | 94            | 5.0765             |                    | 32.71                               | 33.48  | 32.71  |
|  | 90            | 5.0866             |                    | 32.90                               | 33.82  | 32.93  |
| 86   | 5.1088        | 33.33              | 34.15              | 33.39                               |  |  |

**Table S4.** Calculated EoS parameters in the 3rd order Birch–Murnaghan equation with  $K_0'$  fixed 4 for  $Pm\bar{3}n$ -Eu<sub>8</sub>H<sub>46</sub>,  $P6_3/mmc$ -EuH<sub>9</sub>, and  $F\bar{4}3m$ -EuH<sub>9</sub>.  $V_0$  for all europium hydrides corresponds to 100 GPa.

|                         | $Pm\bar{3}n$ -Eu <sub>8</sub> H <sub>46</sub> | $P6_3/mmc$ -EuH <sub>9</sub> | $F\bar{4}3m$ -EuH <sub>9</sub> |
|-------------------------|---|------------------------------|--------------------------------|
| $V_0$ (Å <sup>3</sup> ) | 26.3(1)                                       | 31.9(1)                      | 31.3(1)                        |
| $K_0$ (GPa)             | 471 ± 70                                      | 594 ± 70                     | 699 ± 27                       |
| $K_0'$                  | 4   | 4                            | 4                              |

**Table S5.** Relative energies (in kcal/mol) of the Eu clusters at different spin states.

| Spin state ( $S_{total}$ ) | EuH <sub>28</sub> <sup>19+</sup> | EuH <sub>27</sub> <sup>18+</sup> | EuH <sub>24</sub> <sup>17+</sup> |
|----------------------------|----------------------------------|----------------------------------|----------------------------------|
| 0                          | 207.78                           | 235.09                           | 211.30                           |
| 1                          | 91.34                            | 100.62                           | 112.89                           |
| 2                          | 80.32                            | 84.52                            | 84.40                            |
| 3                          | 0                                | 9.73                             | 64.18                            |
| 4                          | 9.62                             | 0                                | 0                                |

**Table S6.** Occupancies of valence superatomic orbitals.

| MO Type | Hexagonal EuH <sub>9</sub> |          | MO Type | Cubic EuH <sub>9</sub> |          | MO type | $Pm\bar{3}n$ -Eu <sub>8</sub> H <sub>46</sub> |          |
|---------|----------------------------|----------|---------|------------------------|----------|---------|---|----------|
|         | Alpha (↑)                  | Beta (↓) |         | Alpha (↑)              | Beta (↓) |         | Alpha (↑)                                     | Beta (↓) |
| F       | 0.97                       | -        | F       | 0.97                   | -        | F       | 0.98  | -        |
| F       | 0.97                       | -        | F       | 0.97                   | -        | F       | 0.98  | -        |
| F       | 0.97                       | -        | F       | 0.97                   | -        | F       | 0.98  | -        |
| F       | 0.97                       | -        | F       | 0.97                   | -        | F       | 0.98  | -        |
| F       | 0.97                       | -        | F       | 0.96                   | -        | F       | 0.97  | -        |
| F       | 0.97                       | -        | F       | 0.96                   | -        | F       | 0.96  | -        |
| F       | 0.96                       | -        | F       | 0.96                   | -        | F       | 0.96  | -        |
| D       | 0.95                       | 0.77     | D       | 0.79                   | 0.78     | D       | 0.59  | 0.58     |
| D       | 0.78                       | 0.76     | D       | 0.79                   | 0.77     | D       | 0.59  | 0.58     |
| D       | 0.77                       | 0.74     | P       | 0.68                   | 0.70     | D       | 0.59  | 0.56     |
| D       | 0.74                       | 0.72     | P       | 0.68                   | 0.70     | D       | 0.56  | 0.55     |
| D       | 0.72                       | 0.67     | P       | 0.68                   | 0.70     | D       | 0.55  | 0.54     |
| P       | -                          | 0.65     | S       | -                      | 0.65     | P       | -   | 0.54     |

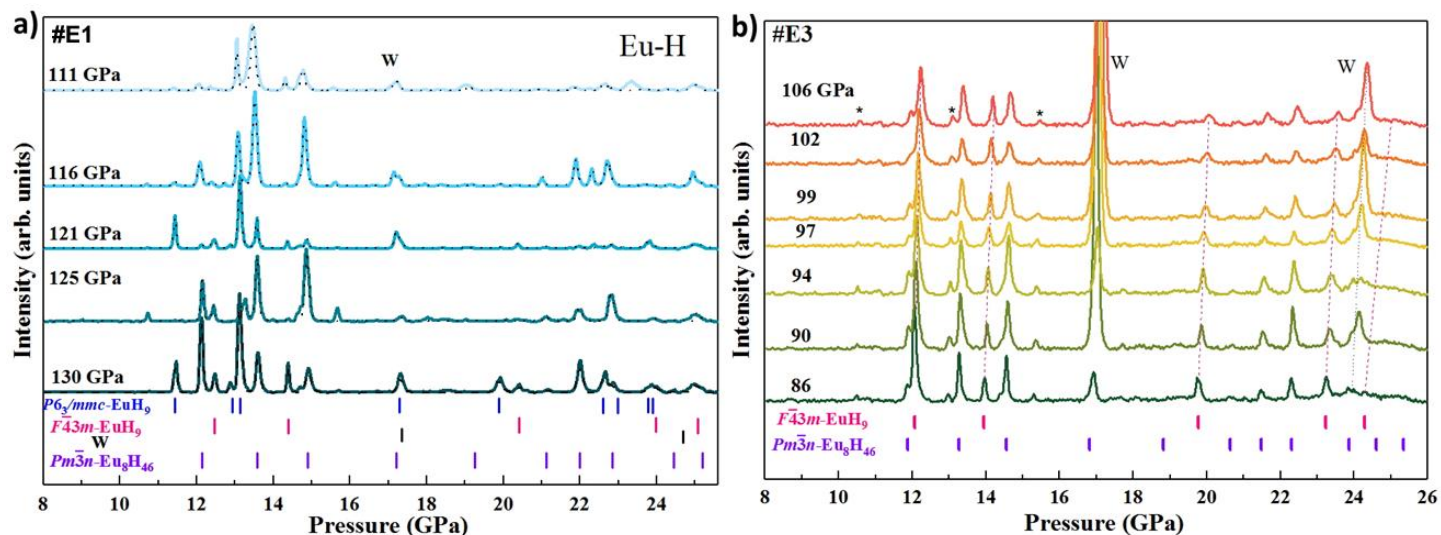


**Figure S2.** Decomposition of Eu polyhydrides after decreasing pressure in cell (a) #E1 and (b) #E3. The XRD patterns were indexed by  $Pm\bar{3}n$ -Eu<sub>8</sub>H<sub>46</sub>,  $P6_3/mmc$ -EuH<sub>9</sub>, and  $F\bar{4}3m$ -EuH<sub>9</sub>. Dash lines are the model fit for the structures in Figures S2a.

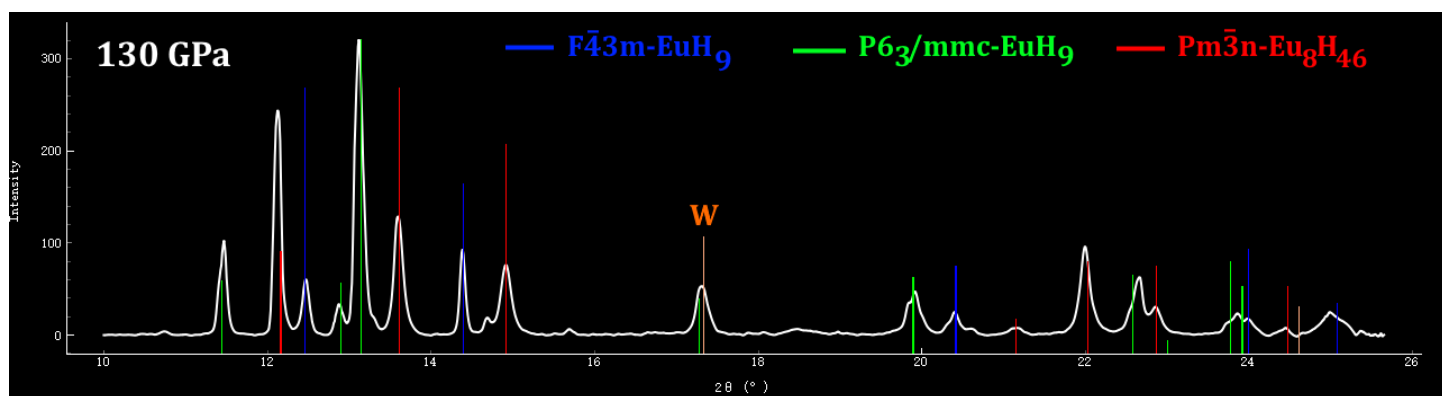


**Figure S3.** Qualitative correlation of the experimental reflections and simulated diffraction patterns of the Eu–H phases at 130 GPa, integrated using Dioptas software.

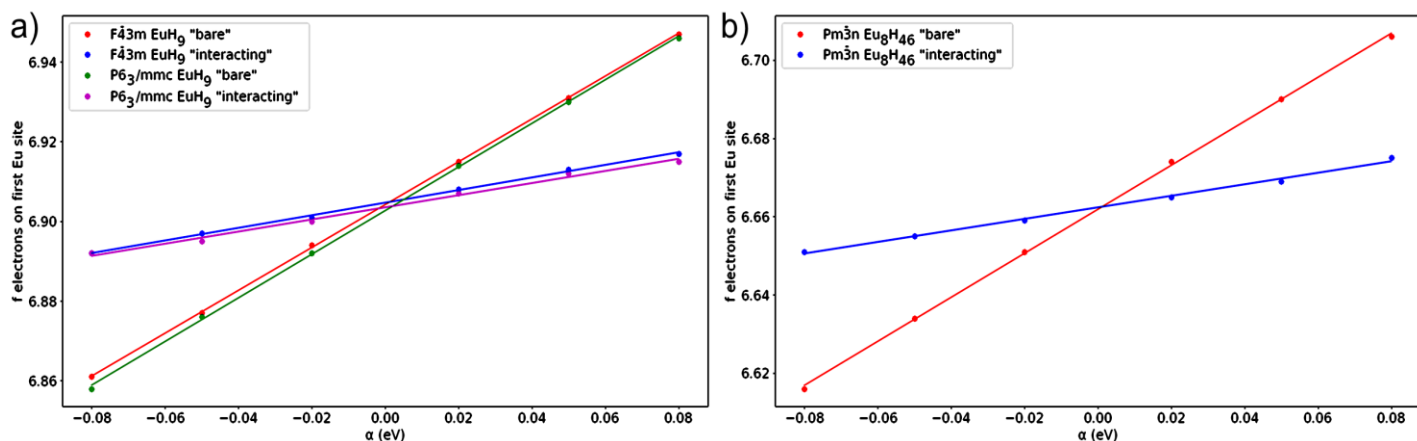


**Figure S4.** Linear response functions for (a) both EuH<sub>9</sub> phases and (b) the Eu<sub>8</sub>H<sub>46</sub> phase. The calculated values are shown by dots; straight lines represent the least squares fit.

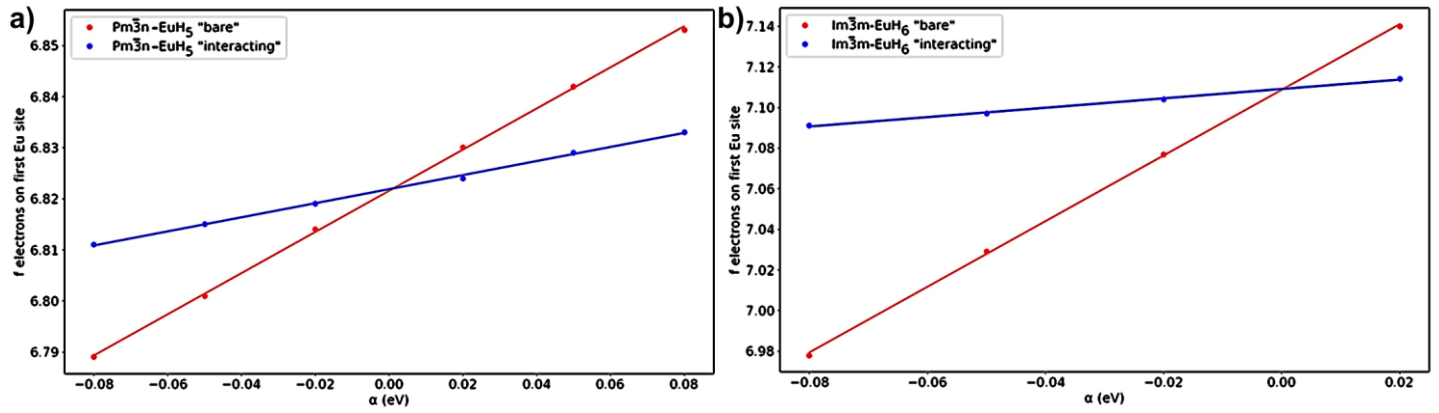


**Figure S5.** Linear response functions for (a)  $\text{EuH}_5$  and (b)  $\text{EuH}_6$  phases. The calculated values are shown by dots; straight lines represent the least squares fit.

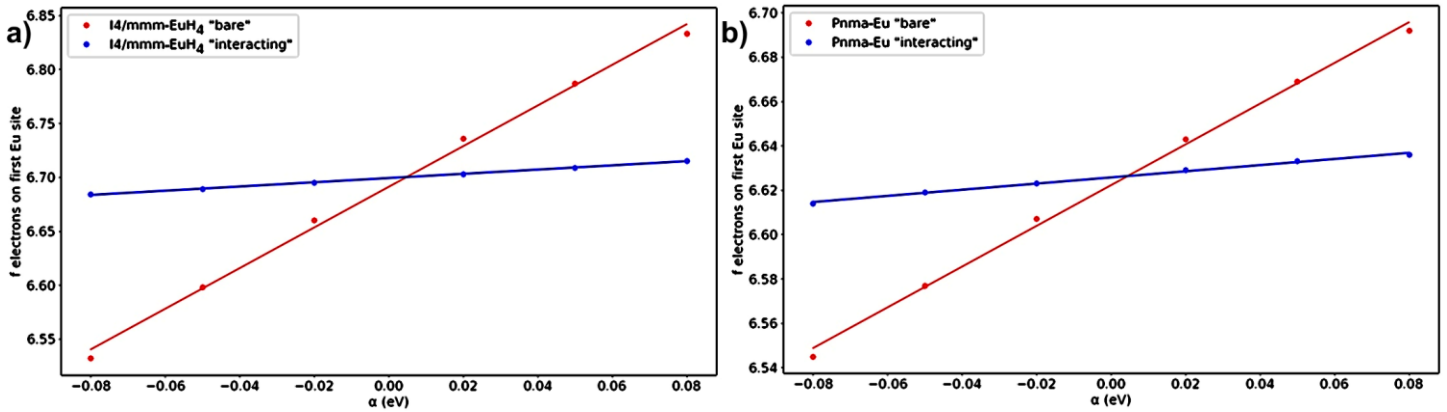


**Figure S6.** Linear response functions for (a) tetragonal  $\text{EuH}_4$  and (b) pure  $\text{Eu}$  at 75 GPa. The calculated values are shown by dots; straight lines represent the least squares fit.

**Table S7.** Linear response functions and calculated  $U$  for the  $\text{Eu-H}$  phases at 130 GPa.

| Phase                                 | “Bare” response ( $\text{eV}^{-1}$ ) | “Interacting” response ( $\text{eV}^{-1}$ ) | $U-J$ (eV) |
|---------------------------------------|--------------------------------------|---|------------|
| $F\bar{4}3m\text{-EuH}_9$             | 0.158                                | 0.537                                       | 4.46       |
| $P6_3/mmc\text{-EuH}_9$               | 0.152                                | 0.547                                       | 4.74       |
| $Pm\bar{3}n\text{-Eu}_8\text{H}_{46}$ | 0.147                                | 0.562                                       | 5.01       |
| $Im\bar{3}m\text{-EuH}_6^*$           | 0.231                                | 1.616                                       | 3.7        |
| $Pm\bar{3}n\text{-EuH}_5$             | 0.138                                | 0.403                                       | 4.8        |
| $I4/mmm\text{-EuH}_4$                 | 0.196                                | 1.884                                       | 4.6        |
| $Pnma\text{-Eu}$ (75 GPa)             | 0.139                                | 0.918                                       | 6.1        |

\*For  $\text{EuH}_6$ , only perturbations up to 0.02 eV were included, because larger perturbations showed high nonlinearity.

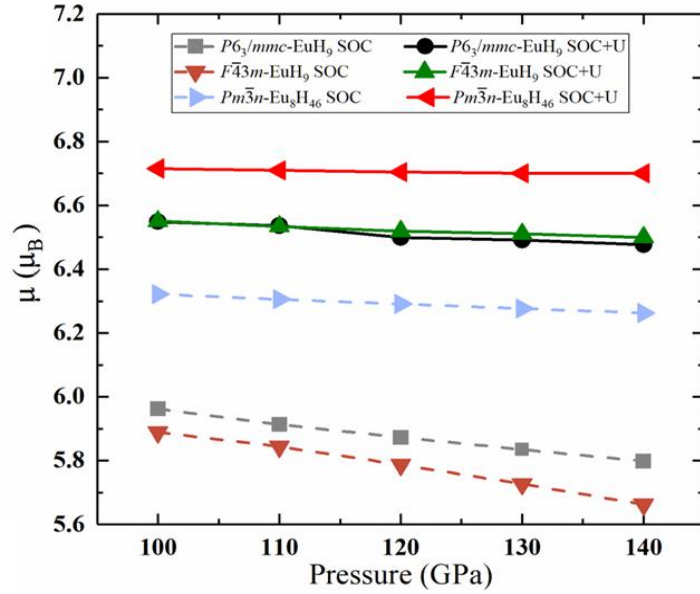


**Figure S7.** Magnetic moments ( $\mu_B$  per 1 Eu atom) of all synthesized Eu-H compounds with and without  $U$ - $J$  and SOC.

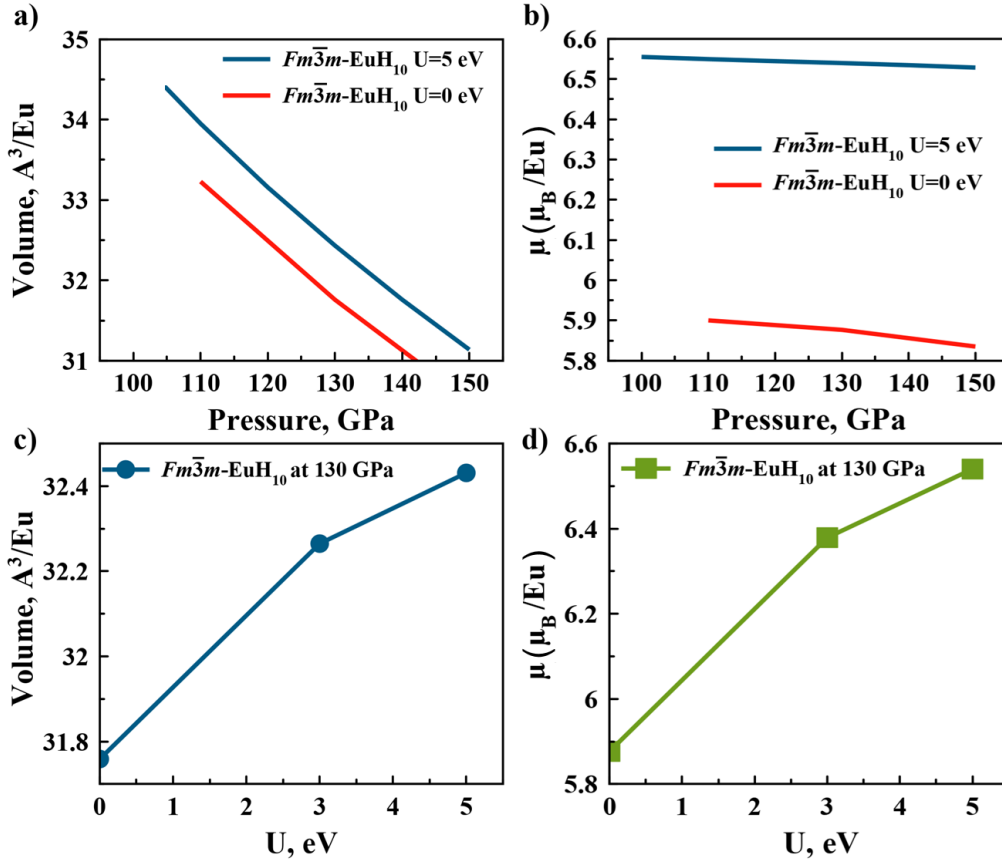


**Figure S8.** (a) Equation of state, (b) magnetic moment per 1 Eu atom, (c) dependence of the unit cell volume  $V$  on the Hubbard-like correction term  $U$ - $J$  at 130 GPa, and (d) dependence of the magnetic moment on  $U$ - $J$  at 130 GPa for the proposed  $Fm\bar{3}m$ -EuH<sub>10</sub>, isostructural to  $Fm\bar{3}m$ -LaH<sub>10</sub>.<sup>38</sup>

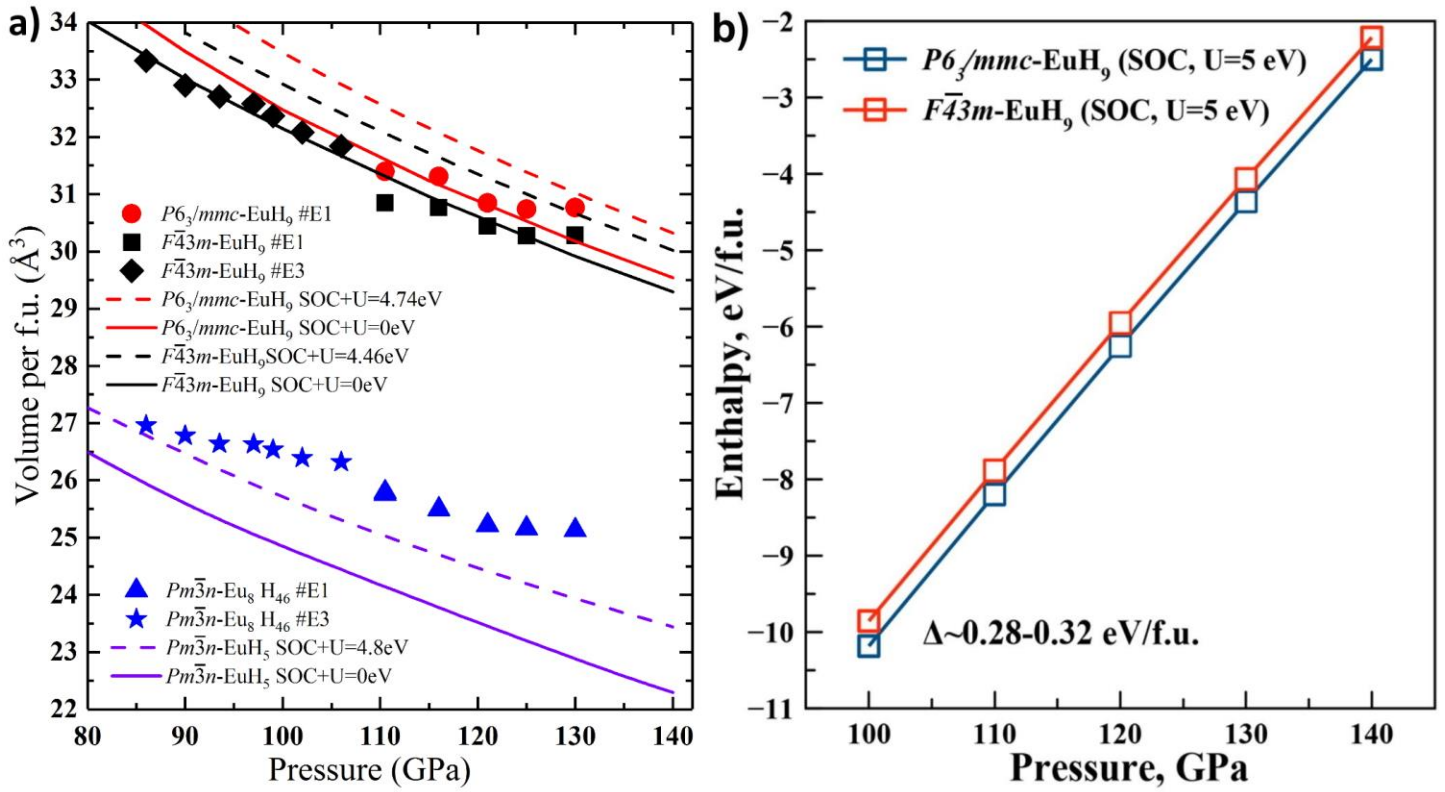


**Figure S9.** (a) Experimental cell volumes of the discovered Eu hydrides and calculated equations of states for  $F\bar{4}3m$ -EuH<sub>9</sub>,  $P6_3/mmc$ -EuH<sub>9</sub>, and proposed  $Pm\bar{3}n$ -Eu<sub>8</sub>H<sub>46</sub><sup>19</sup> with SOC and  $U$ - $J$ . (b) Difference between enthalpies of cubic and hexagonal modifications of EuH<sub>9</sub>.

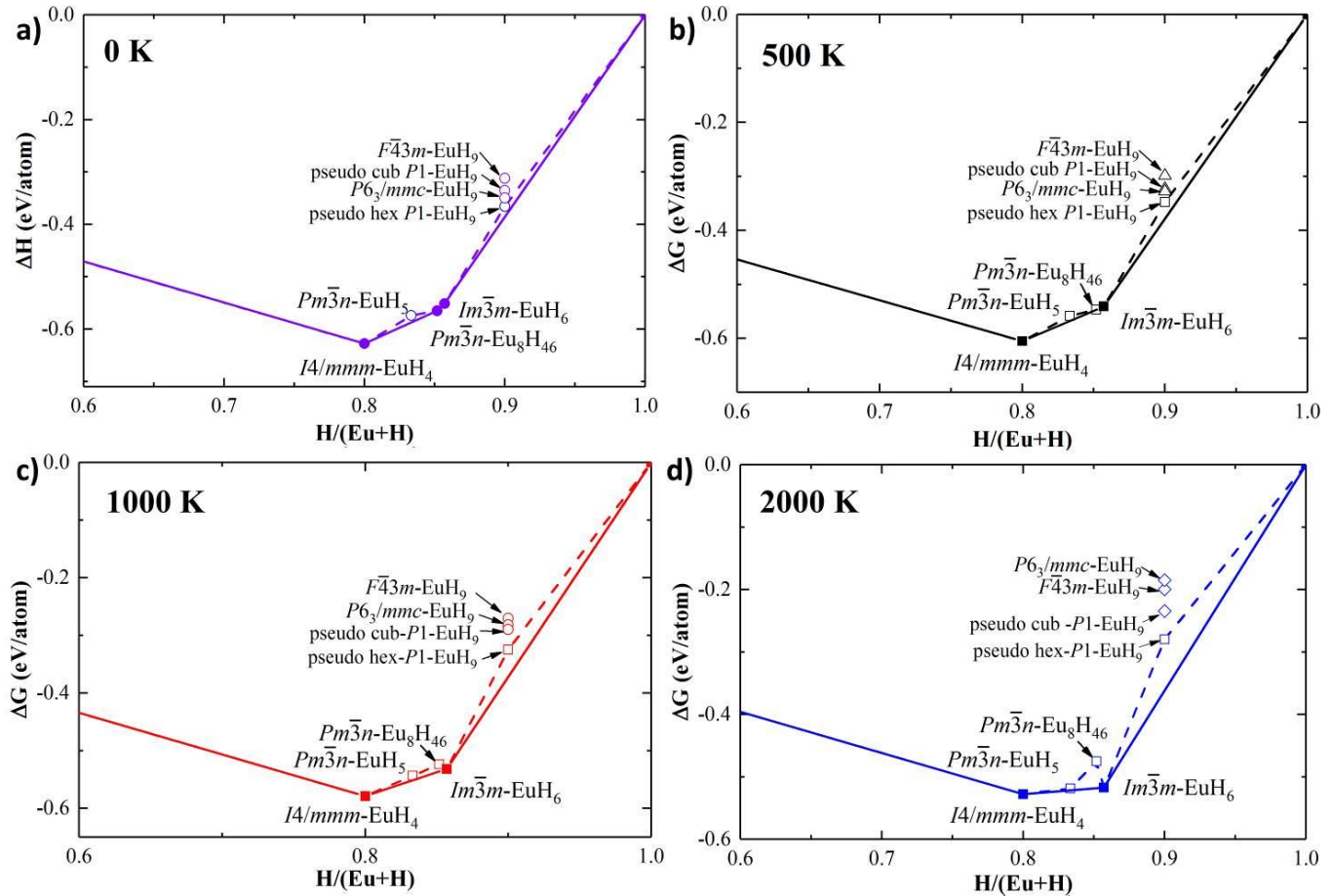


**Figure S10.** Calculated convex hulls of the Eu–H system at 130 GPa and (a) 0 K, (b) 500 K, (c) 1000 K, and (d) 2000 K with the the zero-point energy (ZPE), SOC, and  $U-J$ , specific for each compound (see Table S8).

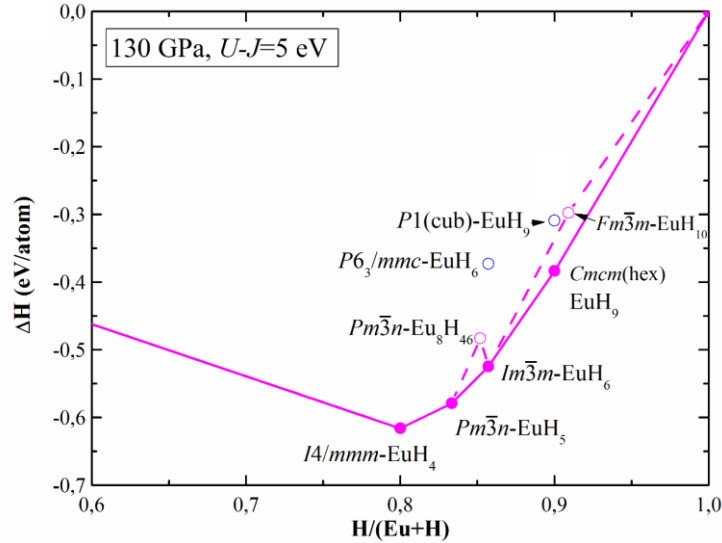


**Figure S11.** Calculated convex hulls of the Eu–H system at 130 GPa for 0 K with the ZPE, SOC, and fixed  $U-J = 5$  eV.

**Table S8.** Enthalpy and energy of formation with and without the ZPE for various Eu–H phases at 130 GPa with SOC and  $U-J$  (from Table S7).

| Phase   | Eu | H  | $x$ (H/Eu+H) | ZPE, eV/Eu | E+ZPE, eV/Eu | $H_{\text{form}}$ , eV/Eu |
|---|----|----|--------------|------------|--------------|---------------------------|
| <i>Pnma</i> -Eu   | 4  | 0  | 0            | 0.0047     | 5.42868      | 0                         |
| <i>I4/mmm</i> -EuH <sub>4</sub>                               | 2  | 8  | 0.8          | 0.15492    | -0.86015     | -0.62783                  |
| <i>Pm</i> $\bar{3}$ <i>n</i> -EuH <sub>5</sub>                | 8  | 40 | 0.83333      | 0.19861    | -0.85113     | -0.57414                  |
| <i>Pm</i> $\bar{3}$ <i>n</i> -Eu <sub>8</sub> H <sub>46</sub> | 8  | 46 | 0.85185      | 0.20604    | -1.94194     | -0.56507                  |
| <i>Im</i> $\bar{3}$ <i>m</i> -EuH <sub>6</sub>                | 2  | 12 | 0.85714      | 0.21108    | -2.90023     | -0.5512                   |
| <i>F</i> $\bar{4}$ <i>3m</i> -EuH <sub>9</sub>                | 4  | 36 | 0.9          | 0.1459     | -3.14065     | -0.31209                  |
| <i>P6</i> $\bar{3}$ / <i>mmc</i> -EuH <sub>9</sub>            | 2  | 18 | 0.9          | 0.19861    | -4.75865     | -0.34938                  |
| pseudocubic EuH <sub>9</sub>                                  | 2  | 1  | 0.9          | 0.34406    | -5.13153     | -0.33561                  |
| pseudohexagonal EuH <sub>9</sub>                              | 4  | 1  | 0.9          | 0.35587    | -4.99386     | -0.36576                  |
| <i>C2/c</i> -H  | 0  | 24 | 1            | 0.00174    | -0.78516     | 0                         |

**Table S9.** Temperature dependence of the Gibbs free energy of formation ( $G_{\text{form}}$ , eV/atom), computed with the ZPE, SOC, and  $U-J$  (from Table S7) for various Eu–H phases at 130 GPa.

| Phase   | Temperature, K |          |          |          |
|---|----------------|----------|----------|----------|
|   | 0              | 500      | 1000     | 2000     |
| <i>Pnma</i> -Eu   | 0              | 0        | 0        | 0        |
| <i>I4/mmm</i> -EuH <sub>4</sub>                               | -0.62783       | -0.60517 | -0.57896 | -0.52767 |
| <i>Pm</i> $\bar{3}$ <i>n</i> -EuH <sub>5</sub>                | -0.57414       | -0.55873 | -0.54337 | -0.51834 |
| <i>Pm</i> $\bar{3}$ <i>n</i> -Eu <sub>8</sub> H <sub>46</sub> | -0.56507       | -0.54654 | -0.5233  | -0.47524 |
| <i>Im</i> $\bar{3}$ <i>m</i> -EuH <sub>6</sub>                | -0.5512        | -0.54096 | -0.53178 | -0.51735 |
| <i>F</i> $\bar{4}$ <i>3m</i> -EuH <sub>9</sub>                | -0.31209       | -0.29836 | -0.2704  | -0.19966 |
| <i>P6</i> $\bar{3}$ / <i>mmc</i> -EuH <sub>9</sub>            | -0.34938       | -0.32308 | -0.28185 | -0.18473 |
| pseudocubic EuH <sub>9</sub>                                  | -0.33561       | -0.31639 | -0.28987 | -0.23441 |
| pseudohexagonal EuH <sub>9</sub>                              | -0.36576       | -0.34746 | -0.32449 | -0.2797  |

|          |   |   |   |   |
|----------|---|---|---|---|
| $C2/c-H$ | 0 | 0 | 0 | 0 |
|----------|---|---|---|---|

**Table S10.** Results of the fixed-composition USPEX search for the best crystal structure of  $Pm\bar{3}n$ -Eu<sub>8</sub>H<sub>46</sub> at 130 GPa.

| ID  | Origin     | Enthalpy | Volume (Å <sup>3</sup> ) | Density (g/cm <sup>3</sup> ) | Fitness (eV) |
|-----|------------|----------|--------------------------|------------------------------|--------------|
| 242 | Permutate  | -32.495  | 189.161                  | 11.079                       | -32.495      |
| 159 | keptBest   | -32.494  | 189.161                  | 11.079                       | -32.494      |
| 70  | keptBest   | -32.488  | 189.161                  | 11.079                       | -32.488      |
| 37  | Seeds      | -32.485  | 189.161                  | 11.079                       | -32.485      |
| 114 | keptBest   | -28.975  | 189.161                  | 11.079                       | -28.975      |
| 197 | keptBest   | -28.474  | 189.161                  | 11.079                       | -28.474      |
| 247 | Permutate  | -27.51   | 186.344                  | 11.247                       | -27.51       |
| 127 | keptBest   | -27.458  | 185.838                  | 11.277                       | -27.458      |
| 8   | Random     | -22.699  | 180.853                  | 11.588                       | -22.699      |
| 271 | softmutate | -22.578  | 181.419                  | 11.552                       | -22.578      |
| 295 | softmutate | -22.225  | 186.344                  | 11.247                       | -22.225      |
| 272 | softmutate | -22.049  | 181.419                  | 11.552                       | -22.049      |
| 42  | RandTop    | -21.987  | 180.853                  | 11.588                       | -21.987      |
| 200 | Heredity   | -21.948  | 184.714                  | 11.346                       | -21.948      |
| 199 | Heredity   | -21.858  | 185.893                  | 11.274                       | -21.858      |
| 131 | softmutate | -21.418  | 186.344                  | 11.247                       | -21.418      |
| 232 | keptBest   | -20.476  | 181.412                  | 11.552                       | -20.476      |
| 324 | Heredity   | -20.359  | 185.809                  | 11.279                       | -20.359      |
| 79  | Heredity   | -20.276  | 185.837                  | 11.277                       | -20.276      |
| 78  | softmutate | -20.162  | 180.825                  | 11.59                        | -20.162      |
| 196 | Random     | -19.428  | 181.706                  | 11.534                       | -19.428      |
| 73  | keptBest   | -19.278  | 180.853                  | 11.588                       | -19.278      |
| 123 | Permutate  | -18.845  | 189.161                  | 11.079                       | -18.845      |
| 284 | Heredity   | -18.6    | 188.341                  | 11.127                       | -18.6        |
| 246 | keptBest   | -18.43   | 180.853                  | 11.588                       | -18.43       |
| 283 | Random     | -18.119  | 182.093                  | 11.509                       | -18.119      |

## Additional Le Bail Refinements

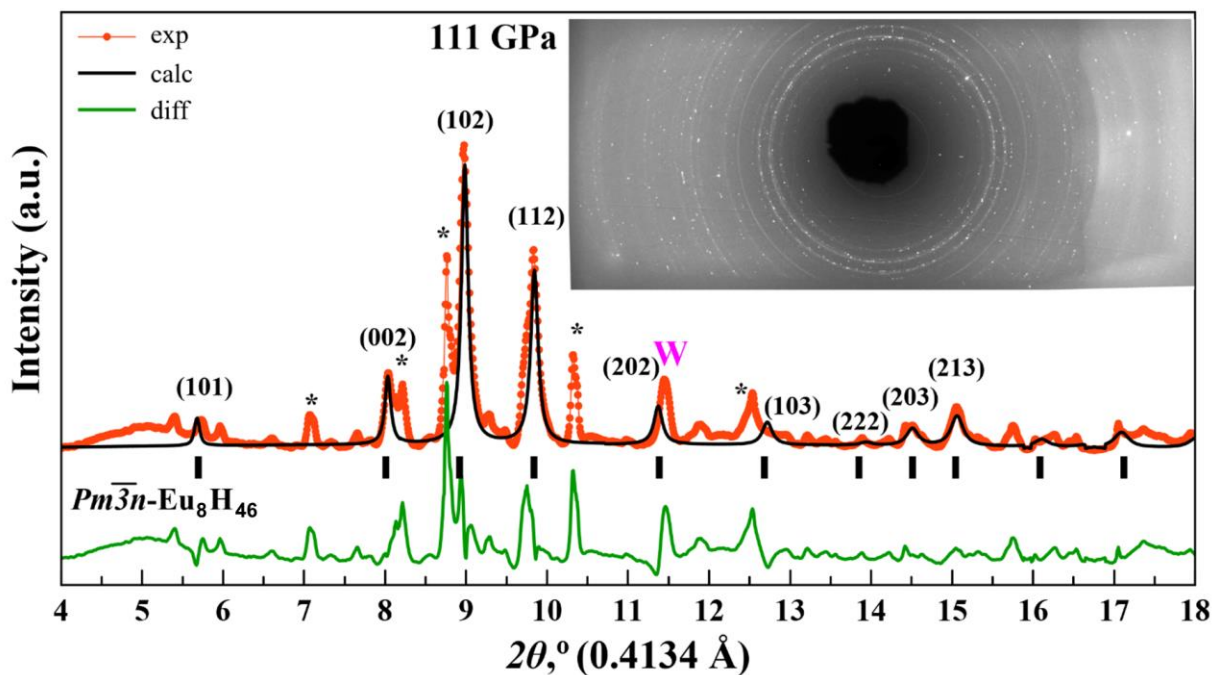


**Figure S12.** Experimental XRD pattern (cell #E1) and the Le Bail refinement of the main phase —  $Pm\bar{3}n$ -Eu<sub>8</sub>H<sub>46</sub> at 111 GPa. Unexplained peaks are marked by asterisks.

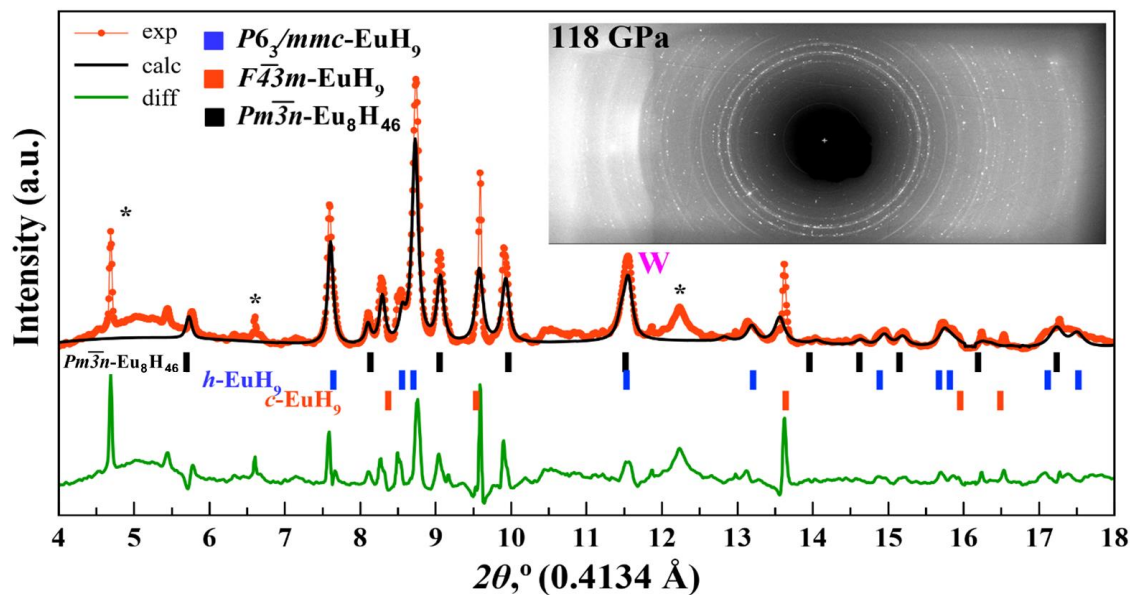


**Figure S13.** Experimental XRD pattern (cell #E1) and the Le Bail refinement of  $F\bar{4}3m$ -EuH<sub>9</sub>,  $P6_3/mmc$ -EuH<sub>9</sub>, and  $Pm\bar{3}n$ -Eu<sub>8</sub>H<sub>46</sub> at 118 GPa. Unexplained peaks are marked by asterisks.

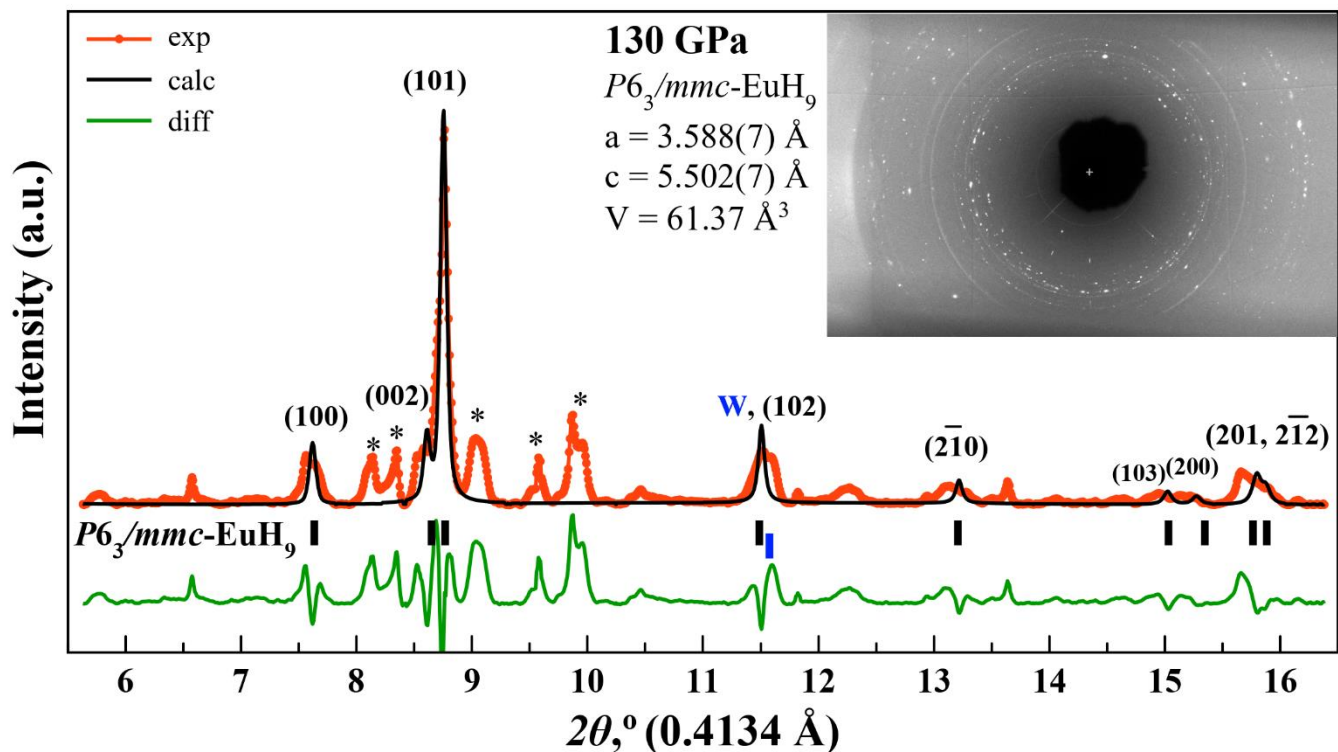


**Figure S14.** Experimental XRD pattern (cell #E1) and the Le Bail refinement of the main phase —  $P6_3/mmc$ -EuH<sub>9</sub> at 130 GPa. Unexplained peaks are marked by asterisks.

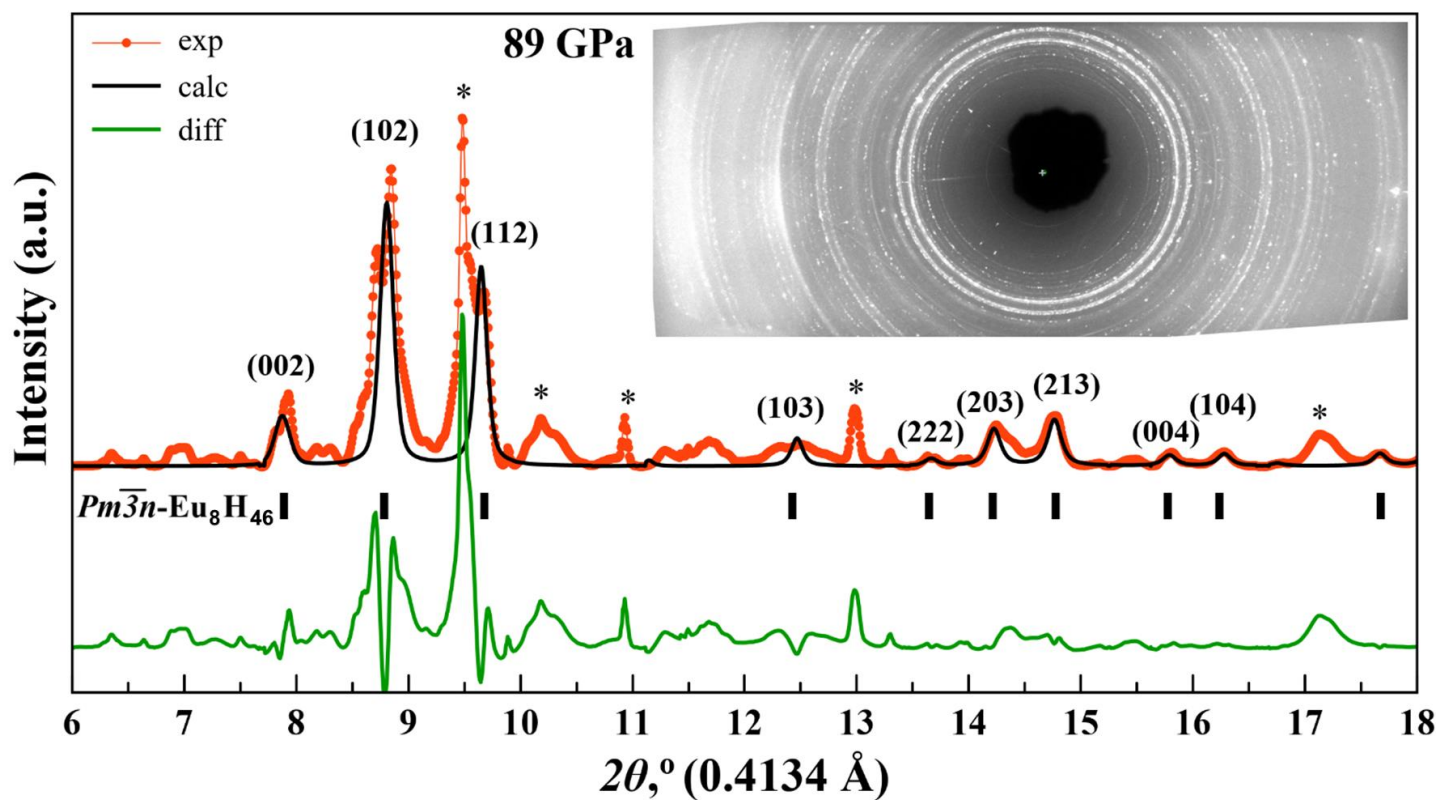


**Figure S15.** Experimental XRD pattern (cell #E2) and the Le Bail refinement of the main phase —  $Pm\bar{3}n$ -Eu<sub>8</sub>H<sub>46</sub> at 89 GPa. Unexplained peaks are marked by asterisks.

## Magnetic Structure

The first step in a detailed study of the magnetic configurations of all europium hydrides is to determine which collinear magnetic ordering is preferable: ferromagnetic (FM) or antiferromagnetic (AFM). If we neglect the spin-orbit coupling, then only the magnitude of magnetic moments is meaningful and we should consider only one possible FM configuration, where the magnetic moments of the Eu atoms point in the same direction. The number of possible AFM configurations, instead, is in principle infinite, since it is always possible to find a new configuration, with half of the spins pointing up and the other half pointing down, by enlarging the unit cell. For this reason, we studied all possible AFM configurations only up to the  $\text{Eu}_4\text{H}_{36}$  supercell for the  $\text{EuH}_9$  stoichiometry. We generated our trial configurations using the derivative structure enumeration library *enumlib*,<sup>39</sup> in which the minimum size able to represent an AFM configuration is always chosen as the size of the unit cell. In other words, if we consider Eu atoms with different spin states as different atomic types, we turn out to always work with primitive cells. We obtained a total of seven AFM configurations for  $F\bar{4}3m\text{-EuH}_9$  and five configurations for  $P6_3/mmc\text{-EuH}_9$ , as shown in Figure 4g,h.

Then we performed a full relaxation of both  $\text{EuH}_9$  phases at 130 GPa without SOC for our eight (seven AFM and one FM) or six (five AFM and one FM) magnetic configurations. All of them successfully completed the process, but after relaxation some of the AFM configurations displayed distorted geometries, with symmetry and enthalpy lower than those of the ideal cubic or hexagonal phase (Table S9).

To explore the magnetic properties of  $Pm\bar{3}n\text{-Eu}_8\text{H}_{46}$ , we examined 15 trial configurations: one FM and 14 AFM (Figure S16). All of them completed relaxation without a change in the orientation of the magnetic moments. As in the case of  $\text{EuH}_9$ , some of the AFM configurations displayed a distorted geometry after relaxation (Table S11). We investigated the space group of all relaxed structures with increasing tolerances and found all distortions becoming negligible if a tolerance of 0.2 is used.

Magnetic anisotropy has been investigated by performing single-point energy calculations with SOC on a FM and an AFM configuration for each of our phases (ideal and distorted ones), with the magnetic moments aligned along seven different directions (Table S12). We expect a little magnetic anisotropy for all phases with  $\text{EuH}_9$  stoichiometry, for which we identified the most stable orientation of the magnetic moments. For  $Pm\bar{3}n\text{-Eu}_8\text{H}_{46}$  we do not expect any magnetic anisotropy since different orientations of the magnetic moments have almost the same enthalpy up to numerical errors.

**Table S11.** Enthalpy and space groups of the trial magnetic structures after full relaxation without SOC at 130 GPa. The space groups were determined with a tolerance of 0.1.

|   | <b>Configuration</b> | <b>Enthalpy (meV/Eu atom)</b> | <b>Space group</b> |
|---|----------------------|-------------------------------|--------------------|
| $F\bar{4}3m$ -EuH <sub>9</sub>                | FM                   | 470.32                        | $F\bar{4}3m$       |
|   | AFM1                 | 0.0                           | $P1$               |
|   | AFM2                 | 440.52                        | $F\bar{4}3m$       |
|   | AFM3                 | 154.85                        | $Imm2$             |
|   | AFM4                 | 165.9                         | $Imm2$             |
|   | AFM5                 | 167.95                        | $Imm2$             |
|   | AFM6                 | 447.47                        | $F\bar{4}3m$       |
|   | AFM7                 | 180.47                        | $Imm2$             |
| $P6_3/mmc$ -EuH <sub>9</sub>                  | FM                   | 197.37                        | $P6_3/mmc$         |
|   | AFM1                 | 215.26                        | $P6_3/mmc$         |
|   | AFM2                 | 213.95                        | $P6_3/mmc$         |
|   | AFM3                 | 0.0                           | $Cmcm$             |
|   | AFM4                 | 59.26                         | $C2$               |
|   | AFM5                 | 8.2                           | $Cmcm$             |
| $Pm\bar{3}n$ -Eu <sub>8</sub> H <sub>46</sub> | FM                   | 0.0                           | $Pm\bar{3}n$       |
|   | AFM1                 | 56.92                         | $Pm\bar{3}n$       |
|   | AFM2                 | 64.78                         | $Pm\bar{3}n$       |
|   | AFM3                 | 64.73                         | $Pm\bar{3}n$       |
|   | AFM4                 | 56.39                         | $Pm\bar{3}n$       |
|   | AFM5                 | 56.68                         | $P4_2/mmc$         |
|   | AFM6                 | 66.69                         | $Pm\bar{3}n$       |
|   | AFM7                 | 66.66                         | $Pm\bar{3}n$       |
|   | AFM8                 | 56.11                         | $P4_2/mmc$         |
|   | AFM9                 | 56.39                         | $Pm\bar{3}n$       |
|   | AFM10                | 66.59                         | $Pm\bar{3}n$       |
|   | AFM11                | 66.63                         | $Pm\bar{3}n$       |
|   | AFM12                | 56.92                         | $Pm\bar{3}n$       |
|   | AFM13                | 64.74                         | $Pm\bar{3}n$       |
| AFM14   | 64.75                | $Pm\bar{3}n$                  |                    |

**Table S12.** Single-point enthalpies of FM and AFM configurations for both  $\text{EuH}_9$  and  $Pm\bar{3}n\text{-Eu}_8\text{H}_{46}$  (including the distorted structures  $P1$ ,  $Imm2$ ,  $Cmcm$ ,  $C2$ ), calculated with SOC and with the magnetic moments aligned along seven different directions at 130 GPa.

| Configuration                         | Enthalpy (meV/atom) |            |            |        |        |            |            |
|---------------------------------------|---------------------|------------|------------|--------|--------|------------|------------|
|                                       | X                   | Y          | Z          | XY     | XZ     | YZ         | XYZ        |
| $P1(\text{cub})\text{-EuH}_9$         |                     |            |            |        |        |            |            |
| FM                                    | -                   | 1.047*     | -          | -      | 0.000* | 0.532*     | 0.791*     |
| AFM1                                  | -                   | 0.617      | -          | 0.158* | -      | 0.430      | 0.115      |
| $Imm2(\text{cub})\text{-EuH}_9$       |                     |            |            |        |        |            |            |
| FM                                    | 26.928              | 26.651     | 27.085     | 26.78  | 26.994 | 26.277     | 26.471     |
| AFM3                                  | 0.871               | 0.833      | 1.392      | 0.849  | 1.131  | <b>0.0</b> | 0.291      |
| $F\bar{4}3m\text{-EuH}_9$             |                     |            |            |        |        |            |            |
| FM                                    | 30.226              | 30.283     | 30.275     | 30.272 | 30.244 | 30.318     | 30.281     |
| AFM2                                  | <b>0.0</b>          | 0.41       | 0.205      | 0.171  | 0.076  | 0.652      | 0.397      |
| $Cmcm(\text{hex})\text{-EuH}_9$       |                     |            |            |        |        |            |            |
| FM                                    | 7.691               | 8.878      | 7.309      | 8.289  | 7.489  | 8.12       | 7.958      |
| AFM3                                  | 0.076               | 1.4        | <b>0.0</b> | 0.722  | 0.01   | 0.827      | 0.548      |
| $C2(\text{hex})\text{-EuH}_9$         |                     |            |            |        |        |            |            |
| FM                                    | 0.563               | <b>0.0</b> | 0.396      | 0.296  | 0.767  | 0.185      | 0.498      |
| AFM4                                  | 6.517               | 5.65       | 6.018      | 6.091  | 6.386  | 5.816      | 6.12       |
| $P6_3/mmc\text{-EuH}_9$               |                     |            |            |        |        |            |            |
| FM                                    | 0.176               | 0.176      | <b>0.0</b> | 0.174  | 0.118  | 0.128      | 0.152      |
| AFM1                                  | 19.372              | 19.371     | 18.4       | 19.368 | 18.855 | 18.874     | 19.028     |
| $Pm\bar{3}n\text{-Eu}_8\text{H}_{46}$ |                     |            |            |        |        |            |            |
| FM                                    | 0.057               | 0.057      | 0.057      | 0.023  | 0.022  | 0.016      | <b>0.0</b> |
| AFM                                   | 57.988              | 58.035     | 58.035     | 58.009 | 58.009 | 58.021     | 57.999     |

“-” means the convergence was not reached after 200 electronic steps.

\* Magnetic moments changed the orientation.

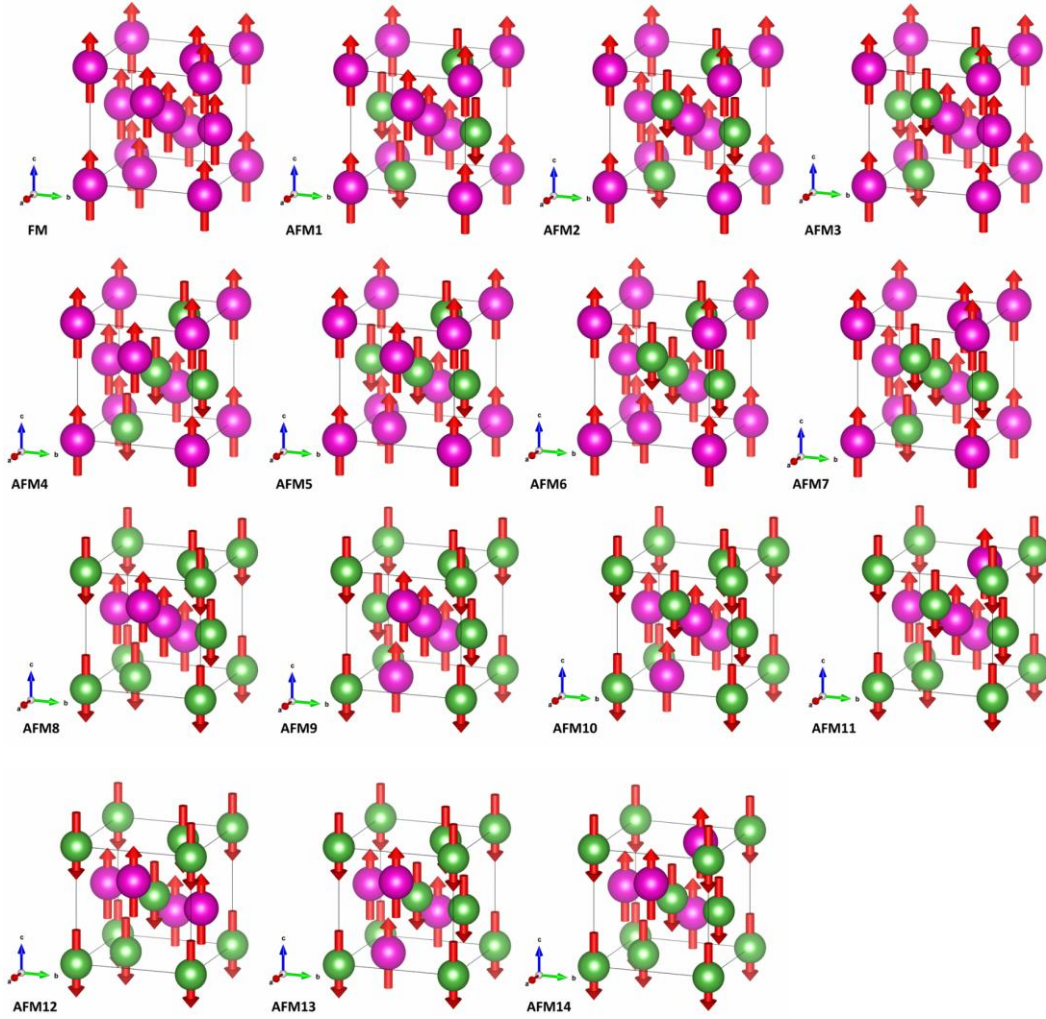


**Figure S16.** 15 trial magnetic configurations for  $Pm\bar{3}n$ -Eu<sub>8</sub>H<sub>46</sub> used in this work.

To study the Néel temperature of  $F\bar{4}3m$ -EuH<sub>9</sub> and the Curie temperature of  $P6_3/mmc$ -EuH<sub>9</sub>, we relaxed two additional independent AFM configurations for each geometry with SOC and the magnetic moments aligned along the  $x$  axis and  $z$  axis, respectively. We used magnetic moments aligned along the  $z$  axis to study the Curie temperature of ferromagnetic  $Pm\bar{3}n$ -Eu<sub>8</sub>H<sub>46</sub>. The final enthalpies and magnetic moment orientations are shown in Table S13, whereas the absolute value of the magnetic moment on each Eu atom after relaxation was always close to  $6.8 \mu_B$  for EuH<sub>9</sub> and  $6.9 \mu_B$  for Eu<sub>8</sub>H<sub>46</sub>.

Taking into account the crystal periodicity, in the unit cell of  $F\bar{4}3m$ -EuH<sub>9</sub> we found 24 links between the Eu atoms at  $3.51 \text{ \AA}$  and 12 links at  $4.96 \text{ \AA}$  at 130 GPa. In the unit cell of  $P6_3/mmc$ -EuH<sub>9</sub>, we found 12 links at  $3.49 \text{ \AA}$  and 12 links at  $3.55 \text{ \AA}$ . Then we modeled the magnetic interaction with the Ising Hamiltonian:

$$H = H_0 - \frac{1}{2}J_1 \sum_{i \neq j} S_i \cdot S_j - \frac{1}{2}J_2 \sum_{i \neq j} S_i \cdot S_j \quad (\text{S1})$$

where  $J_1$  and  $J_2$  are the coupling constants assigned to the two groups of neighbors,  $H_0$  is a constant term which does not depend on the magnetic interaction, and  $S_i$  is  $+1$  or  $-1$ , depending on the spin orientation of the respective Eu atom. This Hamiltonian for EuH<sub>9</sub> takes into account the magnetic interactions only up to the second nearest neighbors.

**Table S13.** Magnetic moment orientations and calculated enthalpies of the three magnetic configurations used for studying the Néel temperature of EuH<sub>9</sub> and of the four magnetic configurations used for studying the Curie temperature of  $Pm\bar{3}n$ -Eu<sub>8</sub>H<sub>46</sub>. +/- mark the direction of magnetic moments along the  $z$  axis.

| $F\bar{4}3m$ -EuH <sub>9</sub>                |     |     |     |     |                        |     |     |     |                        |
|---|-----|-----|-----|-----|------------------------|-----|-----|-----|------------------------|
|   | Eu1 | Eu2 | Eu3 | Eu4 | Enthalpy (meV/Eu atom) |     |     |     |                        |
| FM  | +   | +   | +   | +   | 31.2                   |     |     |     |                        |
| AFM2  | +   | +   | -   | -   | 0.0                    |     |     |     |                        |
| AFM5  | +   | -   | +   | -   | 8.3                    |     |     |     |                        |
| $P6_3/mmc$ -EuH <sub>9</sub>                  |     |     |     |     |                        |     |     |     |                        |
|   | Eu1 | Eu2 | Eu3 | Eu4 | Enthalpy (meV/Eu atom) |     |     |     |                        |
| FM  | +   | +   | +   | +   | 0.0                    |     |     |     |                        |
| AFM1  | +   | -   | +   | -   | 20.0                   |     |     |     |                        |
| AFM3  | +   | +   | -   | -   | 16.7                   |     |     |     |                        |
| $Pm\bar{3}n$ -Eu <sub>8</sub> H <sub>46</sub> |     |     |     |     |                        |     |     |     |                        |
|   | Eu1 | Eu2 | Eu3 | Eu4 | Eu5                    | Eu6 | Eu7 | Eu8 | Enthalpy (meV/Eu atom) |
| FM  | +   | +   | +   | +   | +                      | +   | +   | +   | 0.0                    |
| AFM1  | +   | +   | +   | +   | -                      | -   | -   | -   | 58.0                   |
| AFM5  | +   | -   | +   | +   | -                      | -   | -   | +   | 57.0                   |
| AFM8  | +   | -   | +   | -   | +                      | -   | +   | -   | 66.9                   |

In the primitive cell of Eu<sub>8</sub>H<sub>46</sub>, we found six links between the Eu atoms at 2.95 Å, 24 links at 3.29 Å, and 24 links at 3.61 Å. We modeled the magnetic interaction with the Ising Hamiltonian:

$$H = H_0 - \frac{1}{2}J_1 \sum_{i \neq j} S_i \cdot S_j - \frac{1}{2}J_2 \sum_{i \neq j} S_i \cdot S_j - \frac{1}{2}J_3 \sum_{i \neq j} S_i \cdot S_j \quad (S2)$$

where  $J_1$ ,  $J_2$ , and  $J_3$  are the coupling constants assigned to the three groups of neighbors mentioned above. This Ising Hamiltonian takes into account the magnetic interactions up to the 3rd nearest neighbors for Eu<sub>8</sub>H<sub>46</sub>.

The values of the coupling constants of each phase can be obtained from the enthalpies of our three magnetic configurations by solving the system of equations for  $H_0$ ,  $J_1$ ,  $J_2$ , and  $J_3$ . The critical temperatures in our Heisenberg model were obtained from a Monte Carlo simulation as implemented in the VAMPIRE code.<sup>40</sup> The size of the simulation box was 8×8×8 nm for EuH<sub>9</sub> and 10×10×10 nm for Eu<sub>8</sub>H<sub>46</sub> after the convergence tests, and the transition temperature was found as the value where the normalized mean magnetization length goes below 0.25. The obtained values of the coupling constants and the Néel or Curie temperatures are listed in Tables S14-16, the mean magnetization length is plotted vs. temperature in Figure S17. Obtained normalized  $\mu(T)$  dependencies may be approximated well by the Curie–Weiss type formula  $a+b \cdot (T_{C,N} - T)^{1/2}$ , with  $b = 0.115$  ( $c$ -EuH<sub>9</sub>), 0.066 ( $h$ -EuH<sub>9</sub>) and 0.042 (Eu<sub>8</sub>H<sub>46</sub>).

**Table S14.** Coupling constants (in Joules) and the estimated critical temperatures of both EuH<sub>9</sub> phases and  $Pm\bar{3}n$ -Eu<sub>8</sub>H<sub>46</sub>.

|   | $J_1$ (J per Eu–Eu link) | $J_2$ (J per Eu–Eu link) | $J_3$ (J per Eu–Eu link) | $T_{C,N}$ (K) |
|---|--------------------------|--------------------------|--------------------------|---------------|
| $F\bar{4}3m$ -EuH <sub>9</sub>                | -6.2578e-22              | 1.8056e-23               | -                        | 24            |
| $P6_3/mmc$ -EuH <sub>9</sub>                  | 2.6834e-22               | 5.3336e-22               | -                        | 137           |
| $Pm\bar{3}n$ -Eu <sub>8</sub> H <sub>46</sub> | 2.5042e-21               | 1.4070e-21               | 9.1531e-22               | 336           |

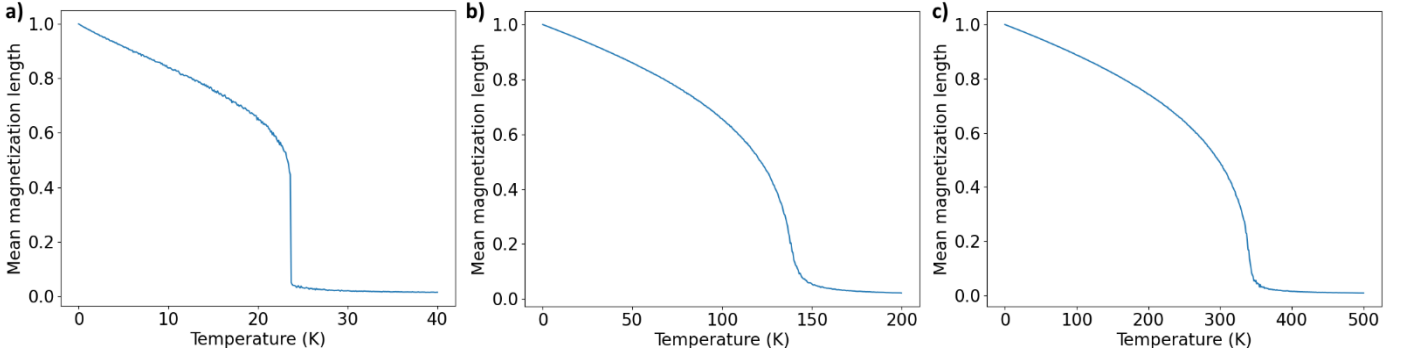


**Figure S17.** Normalized mean magnetization lengths with respect to temperature in (a)  $F\bar{4}3m$ -EuH<sub>9</sub>, (b)  $P6_3/mmc$ -EuH<sub>9</sub>, and (c)  $Pm\bar{3}n$ -Eu<sub>8</sub>H<sub>46</sub> from the Monte Carlo simulations. For antiferromagnetic  $F\bar{4}3m$ -EuH<sub>9</sub> the mean magnetization length of the spin-up channel is displayed.

We chose to truncate the Ising Hamiltonian for the EuH<sub>9</sub> phases to 2nd nearest neighbor interactions on the basis of a convergence test. For  $F\bar{4}3m$ -EuH<sub>9</sub>, we first calculated  $J_1$  from all combinations of enthalpies listed in Table S13, obtaining quite similar values (Table S15). The extension of our Ising Hamiltonian to the 2nd neighbor interactions was dictated only by the possibility of increasing the precision. For  $P6_3/mmc$ -EuH<sub>9</sub>, the values of  $J_1$  for all possible combinations of calculated enthalpies are displayed in Table S15. In one case the system of equations was singular, and in the two remaining cases the calculated values of  $J_1$  are very different. The negative value of  $J_1$  is unphysical because it denotes an AFM ordering, but our system is ferromagnetic. Therefore, we chose to include the second neighbor interactions in our Ising Hamiltonian. We expected them to be of crucial importance in  $P6_3/mmc$ -EuH<sub>9</sub> because they are equally abundant and their distance  $d(\text{Eu-Eu})$  is only 0.06 Å larger compared with the first neighbor interactions. We did not include the 3rd neighbor interactions because their distance, 4.98 Å, is significantly higher than that of the first and the second neighbor interactions and they are equally abundant in the unit cell.

**Table S15.** Values of  $J_1$  (in Joules) for both EuH<sub>9</sub> phases and Eu<sub>8</sub>H<sub>46</sub>, obtained from different combinations of magnetic configurations.

| Phase   | Combination | $J_1$ (J per Eu-Eu link) |
|---|-------------|--------------------------|
| $F\bar{4}3m$ -EuH <sub>9</sub>                | FM, AFM2    | $-6.2578e-22$            |
|   | FM, AFM5    | $-6.1375e-22$            |
|   | AFM2, AFM5  | $-6.6190e-22$            |
| $P6_3/mmc$ -EuH <sub>9</sub>                  | FM, AFM2    | singular                 |
|   | FM, AFM5    | $6.6836e-22$             |
|   | AFM2, AFM5  | $-1.3168e-22$            |
| $Pm\bar{3}n$ -Eu <sub>8</sub> H <sub>46</sub> | FM, AFM1    | singular                 |
|   | FM, AFM5    | $1.8269e-20$             |
|   | FM, AFM8    | $7.1488e-21$             |
|   | AFM1, AFM5  | $-3.0969e-22$            |
|   | AFM1, AFM8  | $9.5606e-22$             |
|   | AFM5, AFM8  | $1.5889e-21$             |

The choice to truncate the Ising Hamiltonian for Eu<sub>8</sub>H<sub>46</sub> to the 3rd nearest neighbor interactions is also the result of a convergence test. In principle, we could have used only the nearest neighbors, calculating  $J_1$  from any

combination of two enthalpies from Table S13 that gives a nonsingular system of equations. The resulting values of  $J_1$  are presented in Table S15. The results are very dependent on the choice of the systems, and in one case we got a negative value of  $J_1$ , which is unphysical because it denotes an AFM ordering, whereas our system is ferromagnetic. In a similar fashion, we could have truncated our Ising Hamiltonian at the 2nd nearest neighbors. In this case we need three relaxed magnetic configurations to calculate  $J_1$  and  $J_2$ . The results for all possible choices are listed in Table S16 together with the respective Curie temperatures from Monte Carlo simulations.

**Table S16.** Values of  $J_1$ ,  $J_2$  (in Joules) and  $T_C$  for  $\text{Eu}_8\text{H}_{46}$  obtained from different combinations of magnetic configurations.

| Phase                                 | Combination      | $J_1$ (J per Eu–Eu link) | $J_2$ (J per Eu–Eu link) | $T_C$ (K) |
|---------------------------------------|------------------|--------------------------|--------------------------|-----------|
| $Pm\bar{3}n\text{-Eu}_8\text{H}_{46}$ | FM, AFM1, AFM5   | 4.3349e–21               | 2.3323e–21               | 376       |
|                                       | FM, AFM1, AFM8   | 2.5042e–21               | 2.3223e–21               | 338       |
|                                       | FM, AFM5, AFM8   | 1.5889e–21               | 2.7799e–21               | 374       |
|                                       | AFM1, AFM5, AFM8 | 1.5889e–21               | 9.4931e–22               | 152       |

For the first three combinations, the obtained values of  $J_2$  are very close to each other. The 2nd nearest neighbor interaction in  $Pm\bar{3}n\text{-Eu}_8\text{H}_{46}$  turns out to be more important than the nearest neighbor interaction because the values of the coupling constants  $J_1$  and  $J_2$  are comparable and the number of second nearest neighbor interactions is four times higher. This is the main reason why the first three Curie temperatures are also close. The results in the last row of Table S14 are most probably due to numerical errors because the enthalpies of the three AFM configurations are relatively close to each other (Table S11). For our calculation of  $T_C$  for  $\text{Eu}_8\text{H}_{46}$ , we chose to take another step forward in accuracy by writing our Ising Hamiltonian up to the 3rd nearest neighbors.

A somewhat more complicated case is pseudo-hexagonal  $Cmcm\text{-EuH}_9$  (Table S12). In order to study the Néel temperature of this phase we checked firstly how much the distances between neighbouring atoms changed with respect to the high-symmetry  $P6_3/mmc$  modification. For computing the Curie temperature of FM  $P6_3/mmc\text{-EuH}_9$ , we wrote the Ising Hamiltonian up to the second nearest neighbors. The situation is different for  $Cmcm\text{-EuH}_9$ , where the first and the second neighbours' distances split into three groups. In the  $Cmcm\text{-Eu}_4\text{H}_{36}$  supercell there are 8 Eu-Eu links at 3.47 Å, 8 links at a distance between 3.52 Å and 3.55 Å and 8 links at 3.61 Å. The next group of neighbours are located at more than 5 Å and therefore we did not take them into account. We figured out that this structural feature of the  $Cmcm$  is responsible for the increased stability of the AFM3 (Figure 4h) magnetic state compared to the FM state of  $P6_3/mmc$  modification.

In the  $Cmcm\text{-Eu}_4\text{H}_{36}$  two more AFM configurations are possible other than AFM3. Together with the FM state, four magnetic configurations are enough to compute three coupling constants ( $J_1$ ,  $J_2$ ,  $J_3$ ) only if they give rise to a non-singular system of equations. Unfortunately, this is not the case for  $Cmcm$  phase, therefore the coupling constants were computed by using the FM state and three independent AFM configurations in the bigger supercell  $\text{Eu}_8\text{H}_{72}$ . As a result we found:  $J_1 = 4.7416 \times 10^{-22}$  J,  $J_2 = 1.1398 \times 10^{-21}$  J,  $J_3 = -1.9388 \times 10^{-21}$  J.

Monte Carlo simulation on the AFM3 magnetic state in the unit cell  $Cmcm\text{-Eu}_4\text{H}_{36}$  using found coupling constants indicates that the AFM3 magnetic ordering is stable only at 0 K, while it collapses at any finite temperature. Among all 76 possible AFM configurations in the supercell  $\text{Eu}_8\text{H}_{72}$  we found that one configuration, denoted here as AFM10, is more stable than the previously described AFM3. However, the Monte Carlo simulation on AFM10 gives the same result as for AFM3. Thus, we can conclude that  $Cmcm\text{-EuH}_9$  does not exhibit magnetism at finite temperatures. This conclusion is very important from the point of view of a possible manifestation of superconductivity in pseudo-hexagonal  $\text{EuH}_9$ .

# Natural Population Analysis

**Table S17.** Occupancies ( $|e|$ ) of localized bonding elements obtained via the SSAdNDP method.

|                                    | <i>P6<sub>3</sub>/mmc</i> -<br><b>CeH<sub>9</sub></b><br>(100 GPa) | <i>F43m</i> -<br><b>PrH<sub>9</sub></b><br>(100 GPa) | <i>P6<sub>3</sub>/mmc</i> -<br><b>PrH<sub>9</sub></b><br>(100 GPa) | <i>P6<sub>3</sub>/mmc</i> -<br><b>NdH<sub>9</sub></b><br>(100 GPa) | <i>Fm3m</i> -<br><b>LaH<sub>10</sub></b><br>(150 GPa) | <i>Fm3m</i> -<br><b>YH<sub>10</sub></b><br>(400 GPa) |
|------------------------------------|--|--|--|--|---|--|
| 1c-2e<br>(s-type lone pairs)       | 1.84   | 1.84   | 1.84   | 1.85   | 1.71  | 1.96   |
| Three 1c-2e<br>(p-type lone pairs) | 1.94   | 1.95   | 1.95   | 1.95   | 1.89  | 1.98   |
| Five <i>nc</i> -2e*                | 1.35-1.25  | 1.44-1.16  | 1.38-1.29  | 1.44-1.21  | 1.65-1.54   | 1.66-1.56  |
| One <i>nc</i> -2e*                 | 1.17   | 1.08   | 1.23   | 1.19   | 1.48  | 1.51   |

\*  $n$  is the number of the hydrogen atoms in the cage.

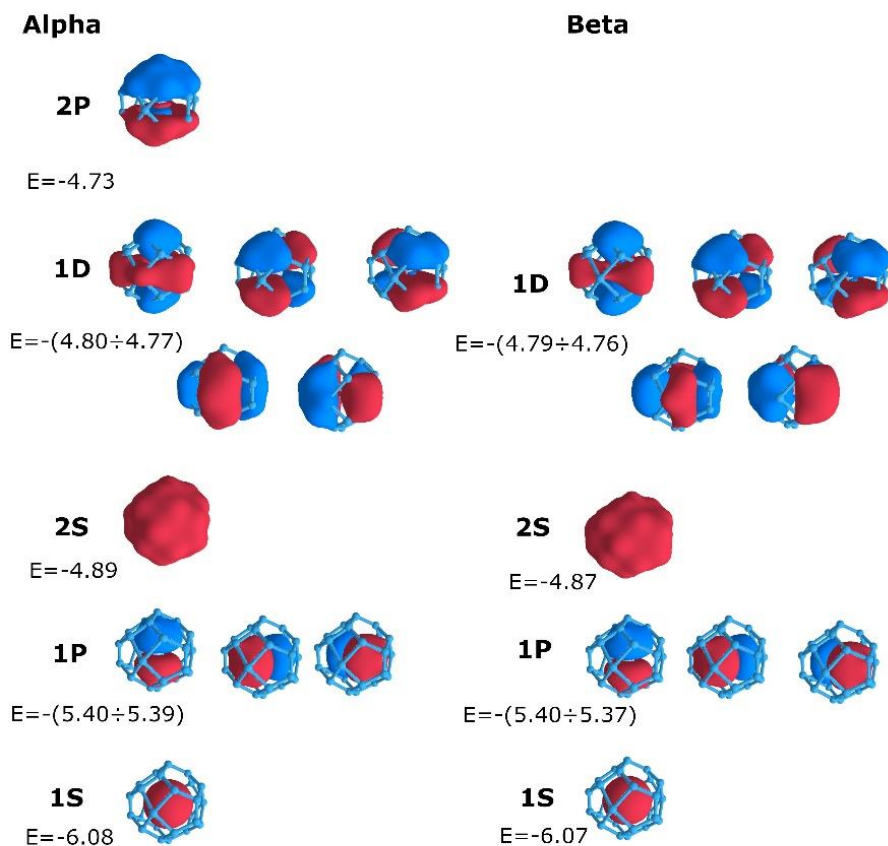


**Figure S18.** Molecular orbitals and energies (Hartree) of  $\text{CeH}_{29}^{20+}$  cluster at 100 GPa.

**Table S18.** Average Bader charges in the investigated europium polyhydrides at 130 GPa.

|                            | <i>Pm3n</i> - <b>Eu<sub>8</sub>H<sub>46</sub></b> | <i>F43m</i> - <b>EuH<sub>9</sub></b> | <i>P6<sub>3</sub>/mmc</i> - <b>EuH<sub>9</sub></b> |
|----------------------------|---|--------------------------------------|--|
| Average charge on Eu atoms | +1.066  | +1.086                               | +1.147   |
| Average charge on H atoms  | -0.185  | -0.121                               | -0.127   |

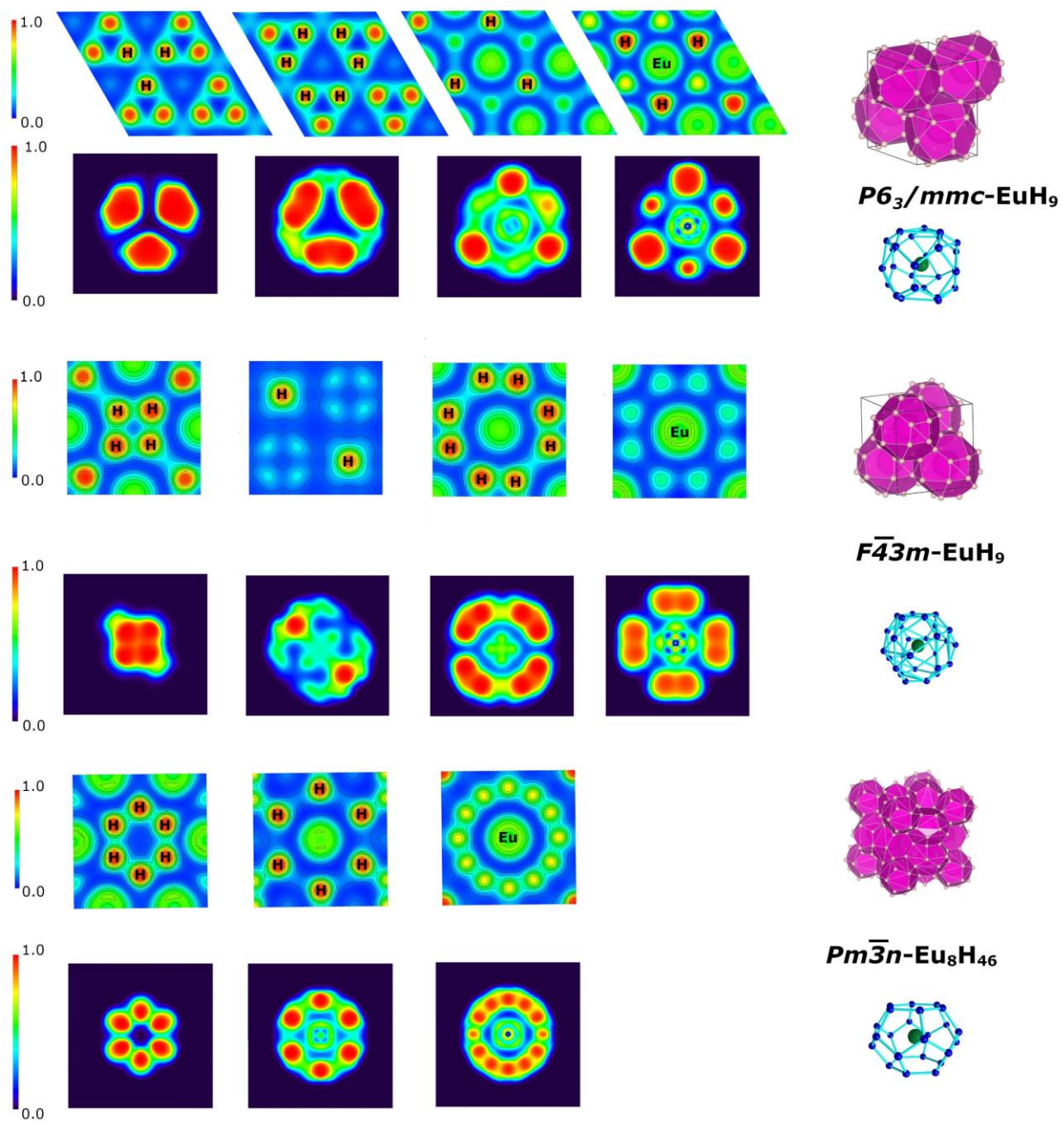


**Figure S19.** Comparison of the ELF plots of the bulk structures of EuH<sub>9</sub> and Eu<sub>8</sub>H<sub>46</sub> and model clusters at 130 GPa.

## Electronic Band Structure

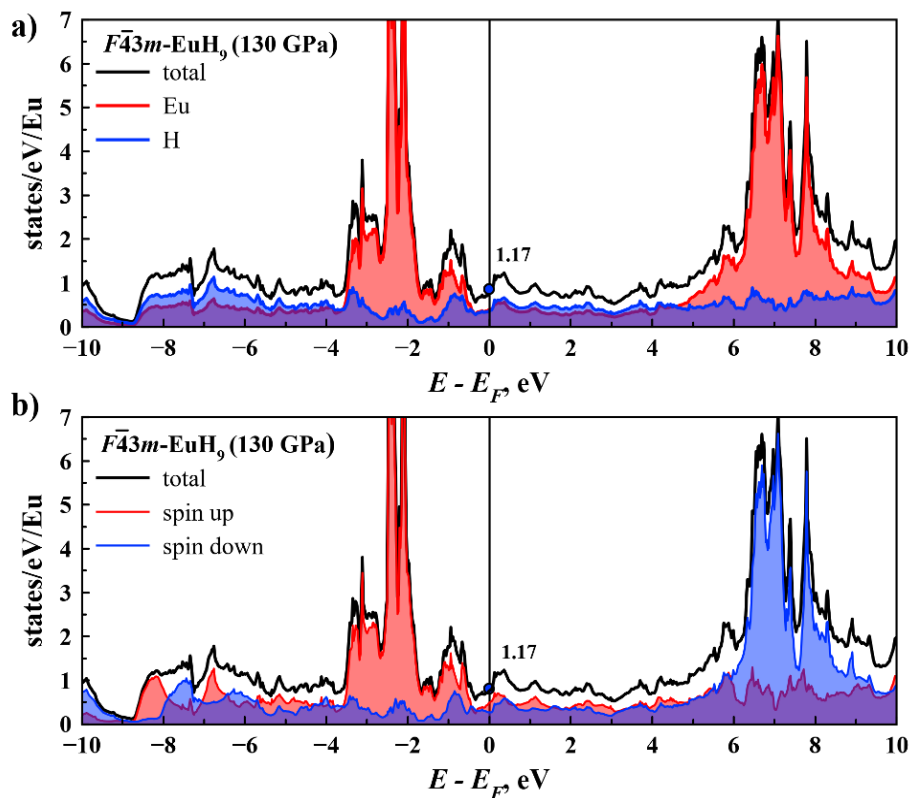


**Figure S20.** Electron density of states (DOS) of  $F\bar{4}3m$ -EuH<sub>9</sub> at 130 GPa per 1 Eu atom (DFT+U). (a) Contributions of the Eu and H atoms to the total DOS. (b) Contributions of different spin orientations to the total DOS.

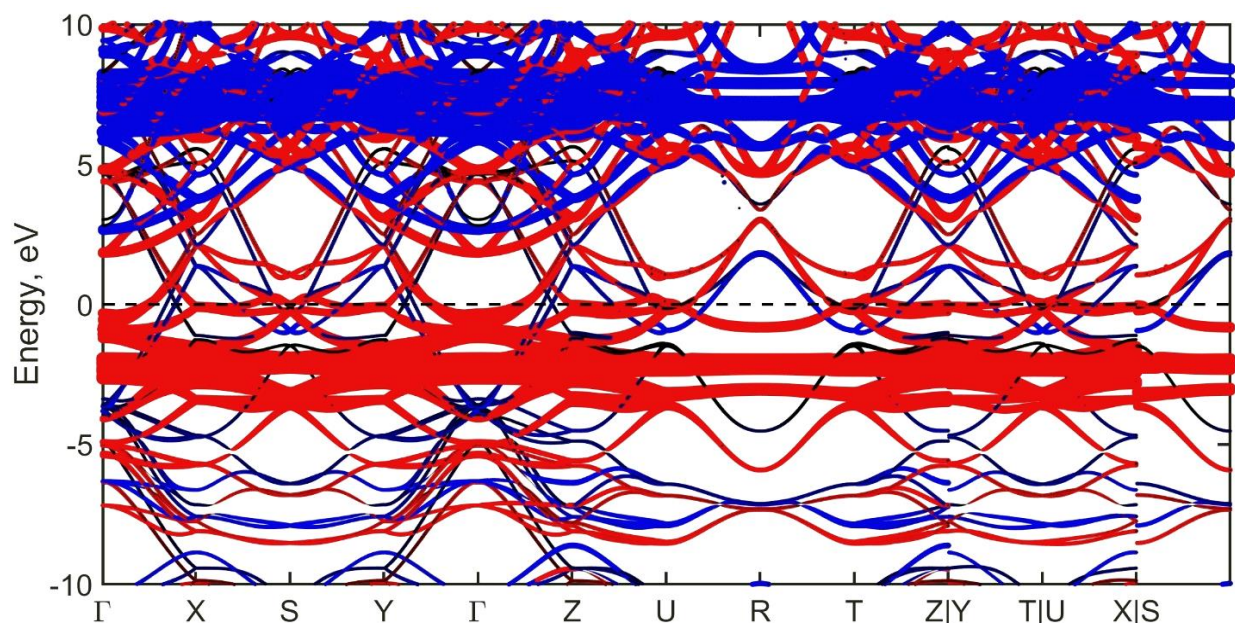


**Figure S21.** Spin-resolved electron band structure (DFT+U) of  $F\bar{4}3m$ -EuH<sub>9</sub> at 130 GPa. Bands of Eu are shown in red (spin up) and blue (spin down), bands of H - in black.

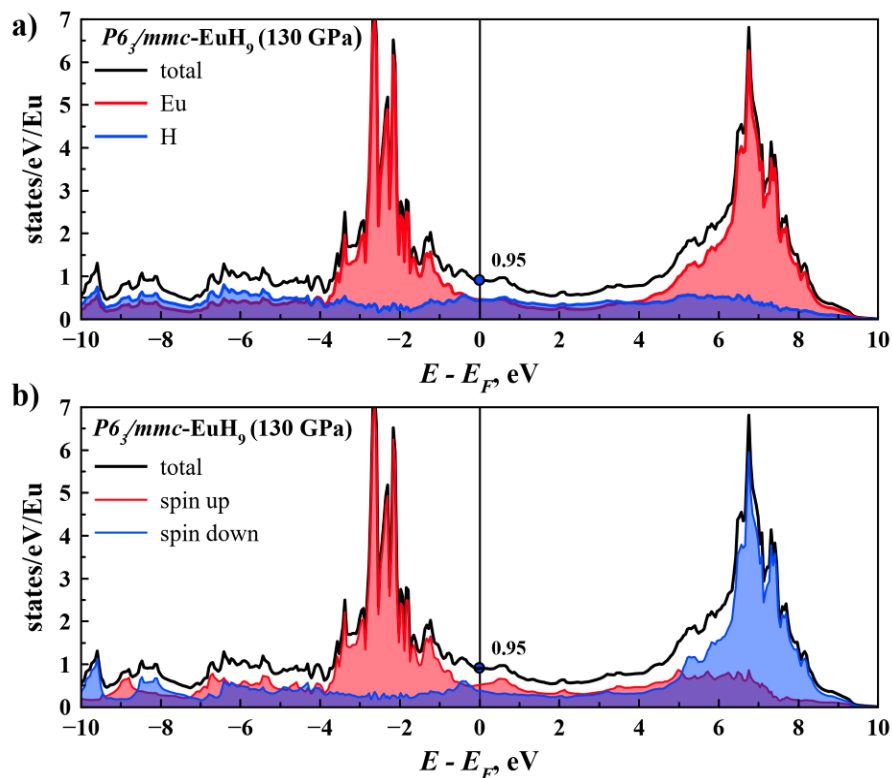


**Figure S22.** Electron density of states (DOS) of  $P6_3/mmc$ -EuH<sub>9</sub> at 130 GPa per 1 Eu atom. (a) Contributions of the Eu and H atoms to the total DOS. (b) Contributions of different spin orientations to the total DOS.

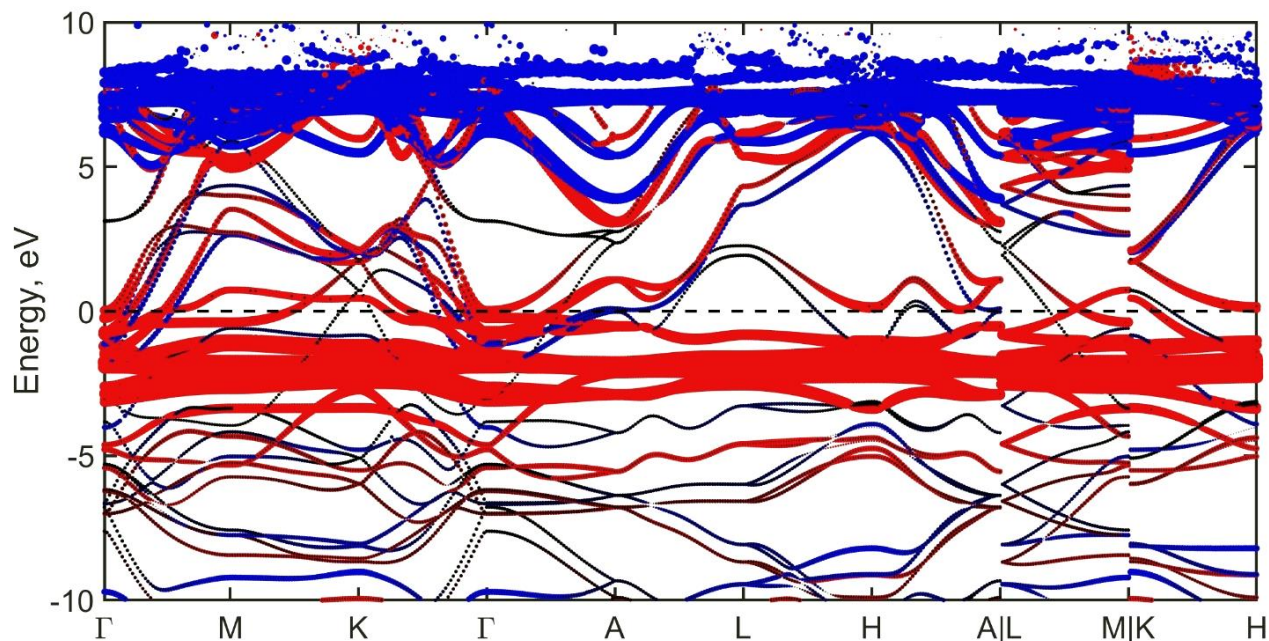


**Figure S23.** Spin-resolved electron band structure of  $P6_3/mmc$ -EuH<sub>9</sub> at 130 GPa. Bands of Eu are shown in red (spin up) and blue (spin down), bands of H presents in black.

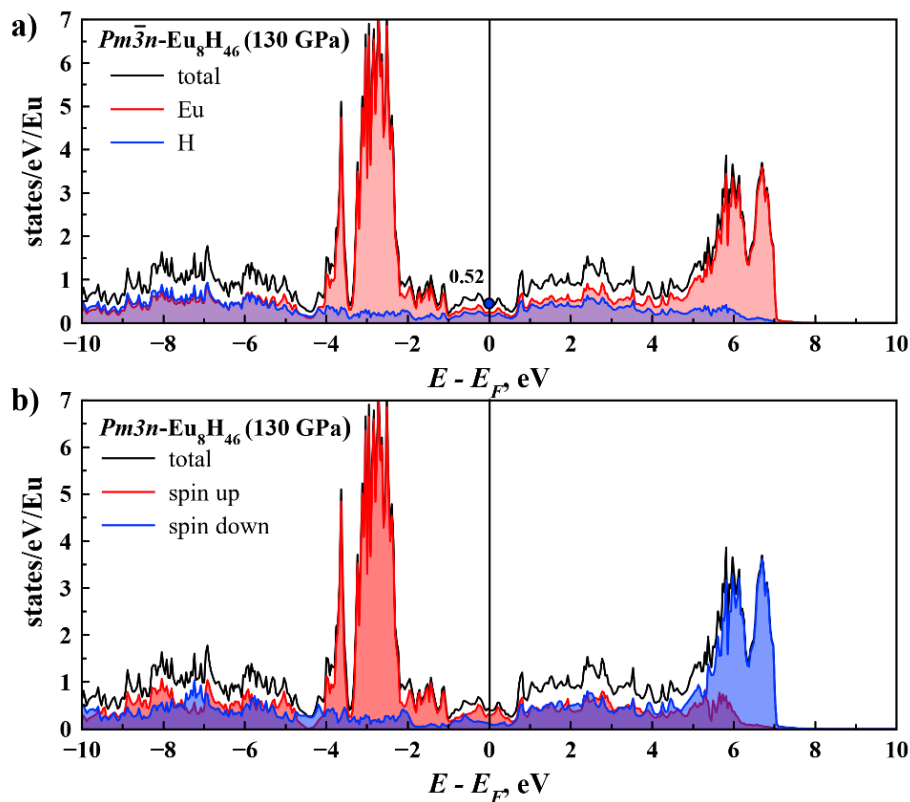


**Figure S24.** Electron density of states (DOS) of  $Pm\bar{3}n\text{-Eu}_8\text{H}_{46}$  at 130 GPa per 1 Eu atom. (a) Contributions of the Eu and H atoms to the total DOS. (b) Contributions of different spin orientations to the total DOS.

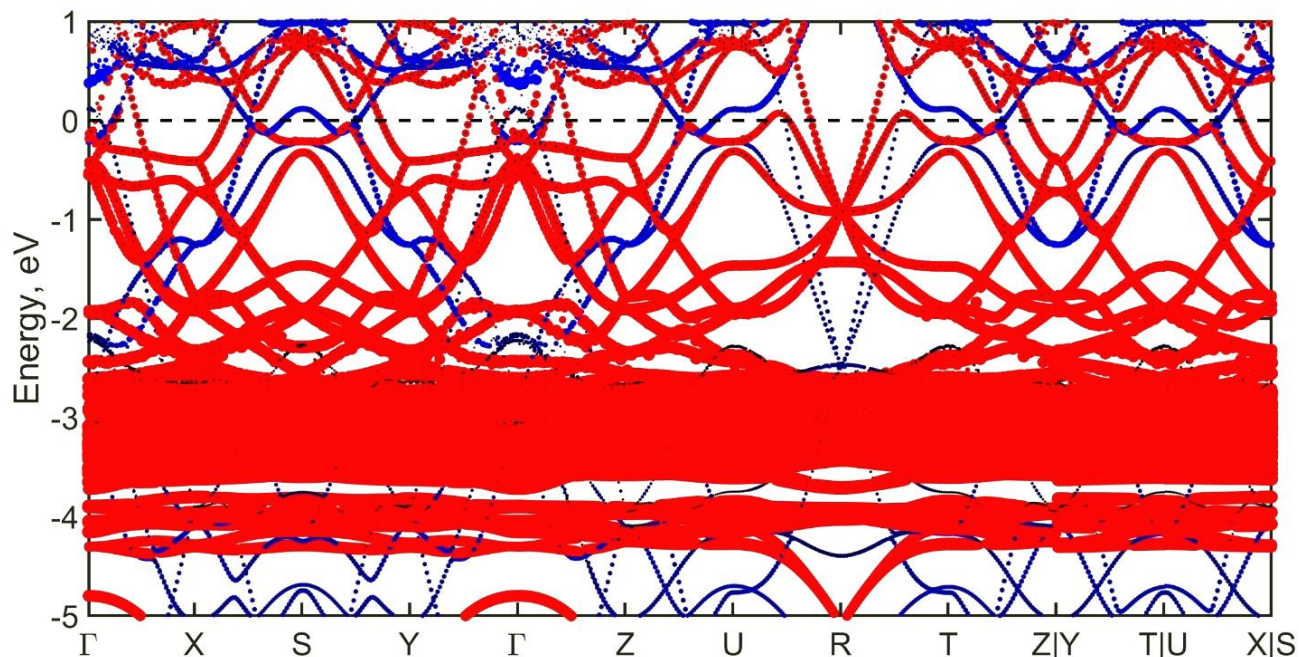


**Figure S25.** Spin-resolved electron band structure of  $Pm\bar{3}n\text{-Eu}_8\text{H}_{46}$  at 130 GPa. Bands of Eu are shown in red (spin up) and blue (spin down), bands of H presents in black.

# Phonon Spectra

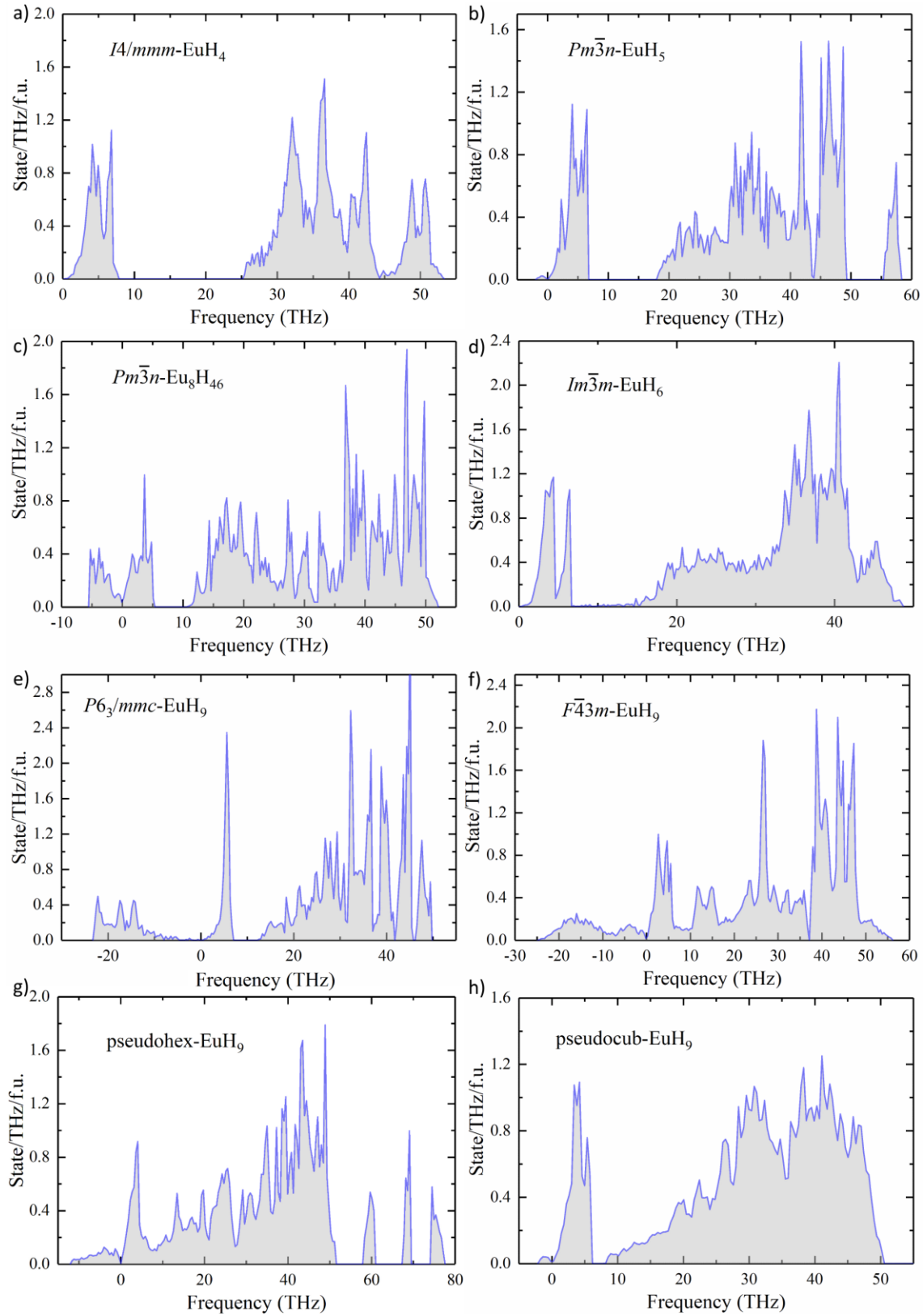


**Figure S26.** Phonon density of states for various Eu–H phases at 130 GPa with SOC and corresponding  $U$ – $J$  (Table S7). Almost all spectra have an imaginary part associated with the distortion of ideal high-symmetry structures or with bad convergence within the selected pseudopotentials. Ideal  $\text{EuH}_9$  phases are unstable, whereas distorted  $P1$ - $\text{EuH}_9$  has much smaller number of imaginary frequencies. Ideal  $Pm\bar{3}n$ - $\text{Eu}_8\text{H}_{46}$  also undergoes distortion.

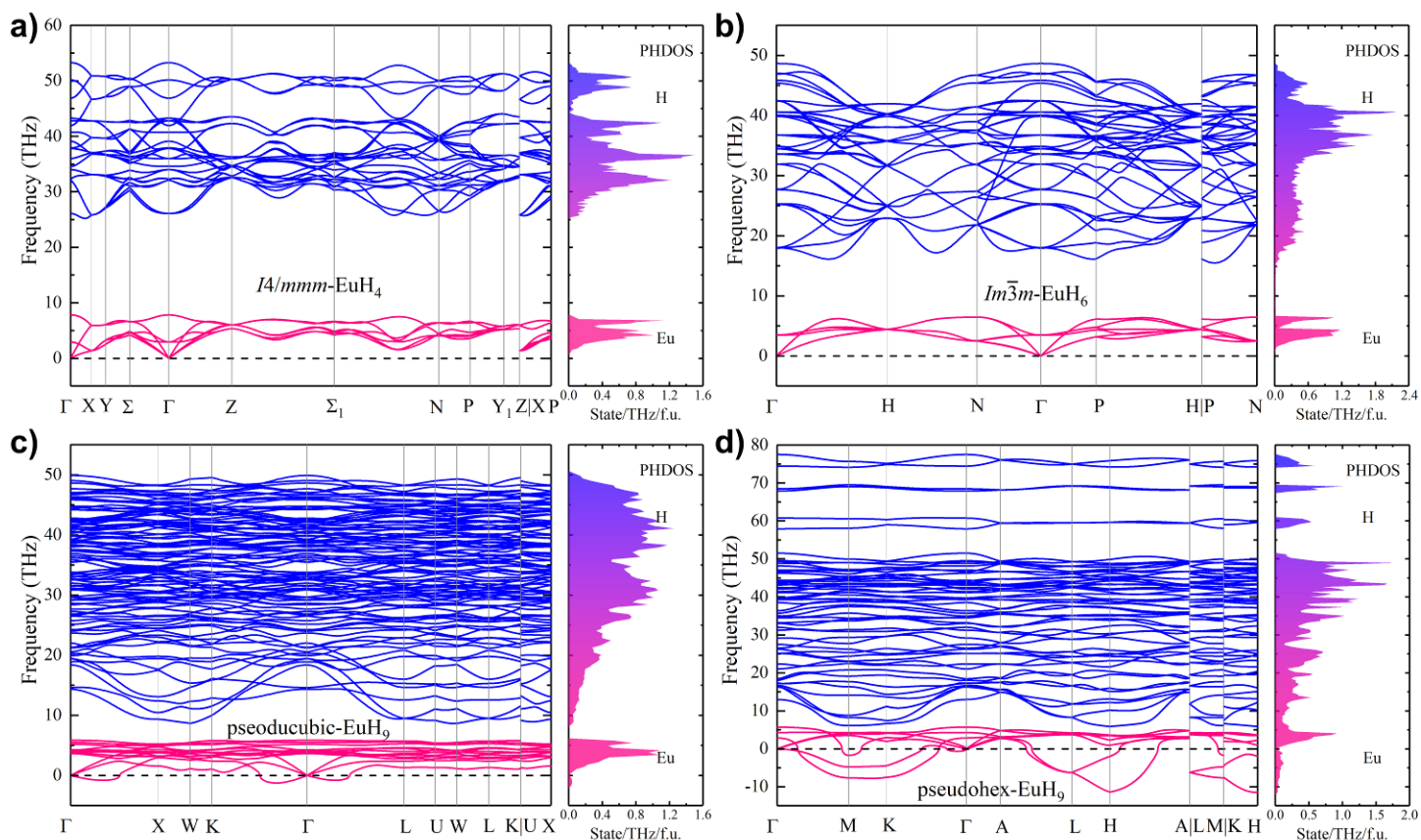


**Figure S27.** Phonon band structure of various Eu hydrides at 130 GPa with SOC and corresponding  $U$ – $J$  (Table S7). Almost all spectra have an imaginary part associated with distortion of ideal high-symmetry structures or with bad convergence within the selected PPs.

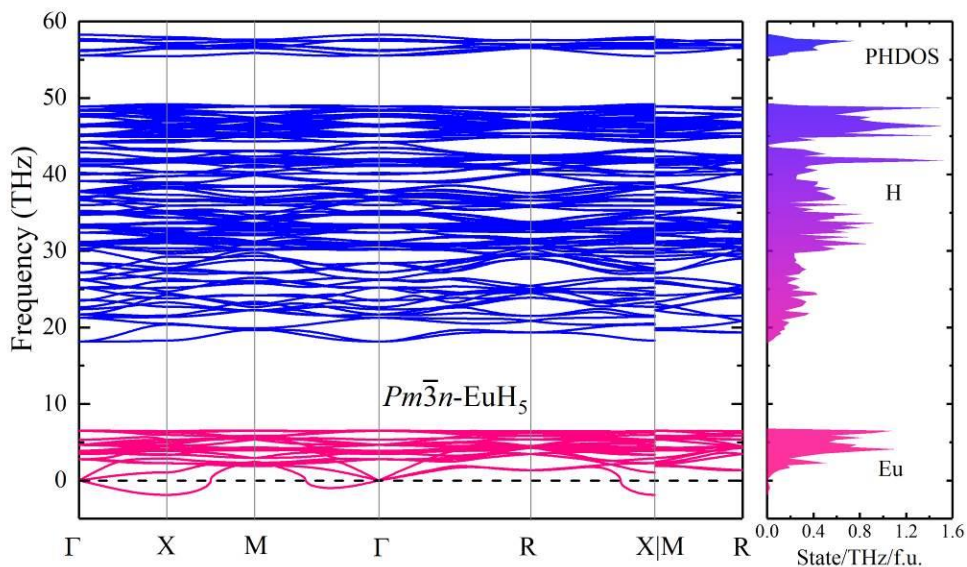


**Figure S28.** Phonon band structure of  $Pm\bar{3}n$ -EuH<sub>5</sub> at 130 GPa with SOC and corresponding  $U$ – $J$  (Table S7).

## Anharmonic Calculations

The dynamic stability and phonon density of states of the europium hydrides were studied using classical molecular dynamics and interatomic potential based on machine learning. We used the Moment Tensor Potential (MTP).<sup>41</sup> It has been demonstrated that the MTP can be used to calculate the phonon properties of materials.<sup>41</sup> Moreover, within this approach we can explicitly take into account the anharmonicity of hydrogen vibrations.

To train the potential, we first simulated studied europium hydrides in quantum molecular dynamics in an NPT ensemble at 130 GPa and 2000 K, with a duration of 5 picoseconds using the VASP code.<sup>13-15</sup> We used the PAW PBE pseudopotentials for the H and Eu atoms,  $2\pi \times 0.06 \text{ \AA}^{-1}$   $k$ -mesh with a cutoff energy of 400 eV, and a  $2 \times 2 \times 1$  supercell with 80 atoms.

For training of the MTP, sets of both  $\text{EuH}_9$  and  $\text{Eu}_8\text{H}_{46}$  structures were chosen using active learning.<sup>42</sup> We checked the dynamical stability of studied europium hydrides with the obtained MTPs via several runs of molecular dynamics calculations at 300 K and 130 GPa. First, the NPT dynamics simulations were performed in a supercell with 960 atoms for 40 picoseconds. During the last 20 picoseconds, the cell parameters were averaged. At the second step, the coordinates of the atoms were averaged within the NVT dynamics with a duration of 20 picoseconds and the final structure was symmetrized. The space groups of both  $\text{EuH}_9$  and  $\text{Eu}_8\text{H}_{46}$  were retained, only the lattice parameters were slightly changed.

Then, for the structures of europium polyhydrides relaxed at 130 GPa and 300 K, the phonon density of states was calculated within the MTP using the velocity autocorrelator (VACF) separately for each type of atoms:<sup>43</sup>

$$g(\vartheta) = 4 \int_0^\infty \cos(2\pi\vartheta t) \frac{\langle \vartheta(0)\vartheta(t) \rangle}{\langle \vartheta(0)^2 \rangle} dt \quad (\text{S3})$$

where  $\vartheta$  is the frequency. The calculations were carried out in a  $20 \times 20 \times 20$  supercell. The velocity autocorrelator was calculated using molecular dynamics, then the phonon DOS was obtained (Figure S29-31).

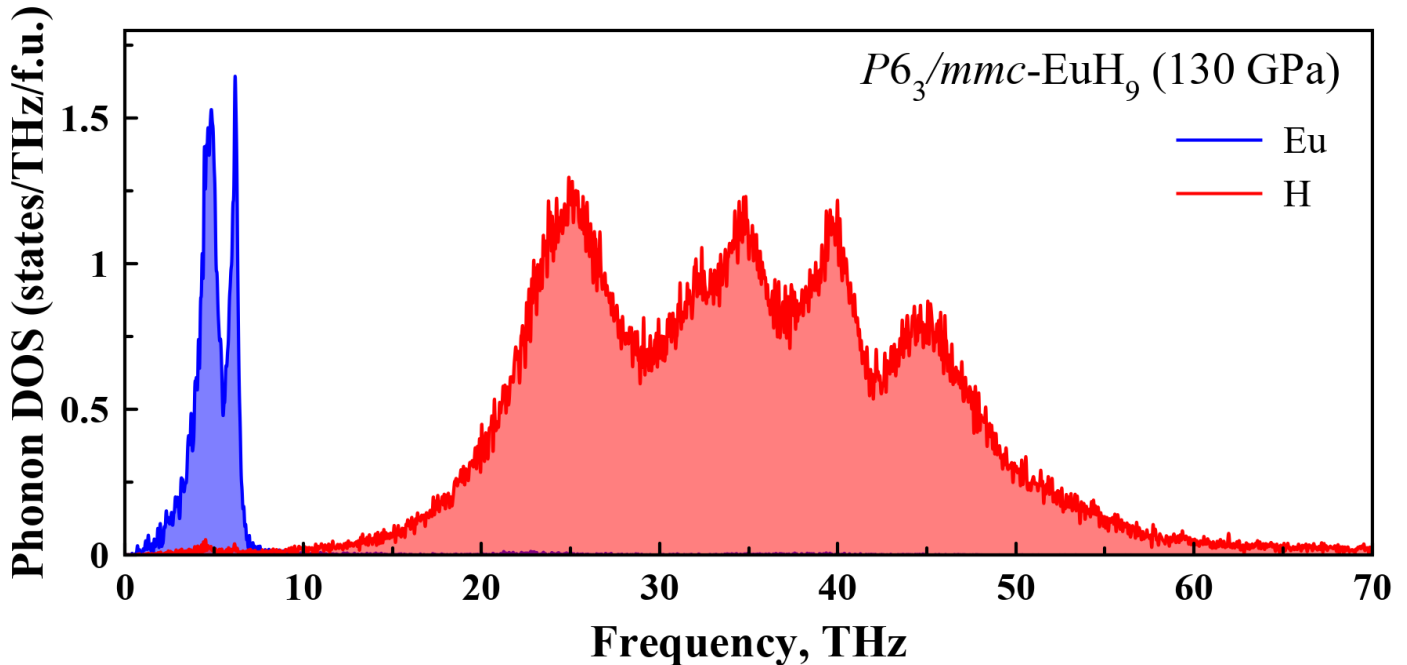


**Figure S29.** Anharmonic phonon density of states of  $P6_3/mmc$ - $\text{EuH}_9$  at 130 GPa and 300 K.

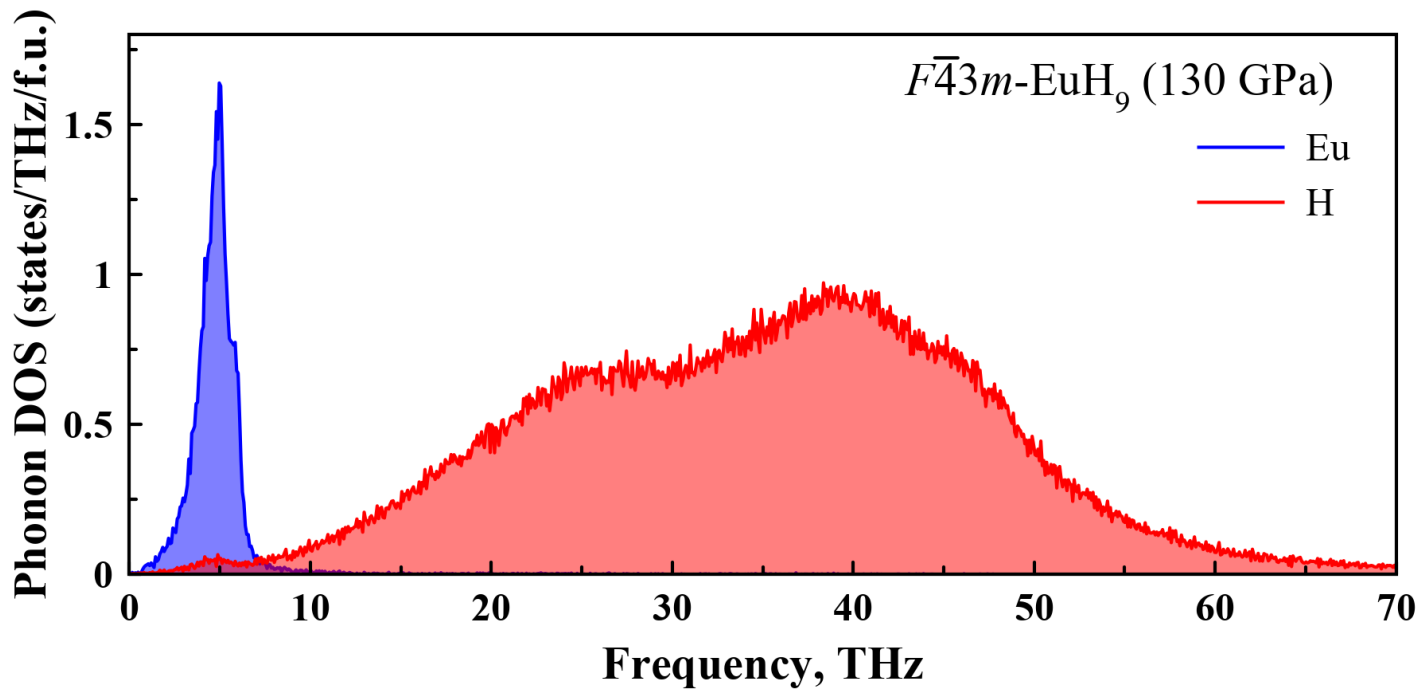


Figure S30. Anharmonic phonon density of states of  $F\bar{4}3m$ -EuH<sub>9</sub> at 130 GPa and 300 K.

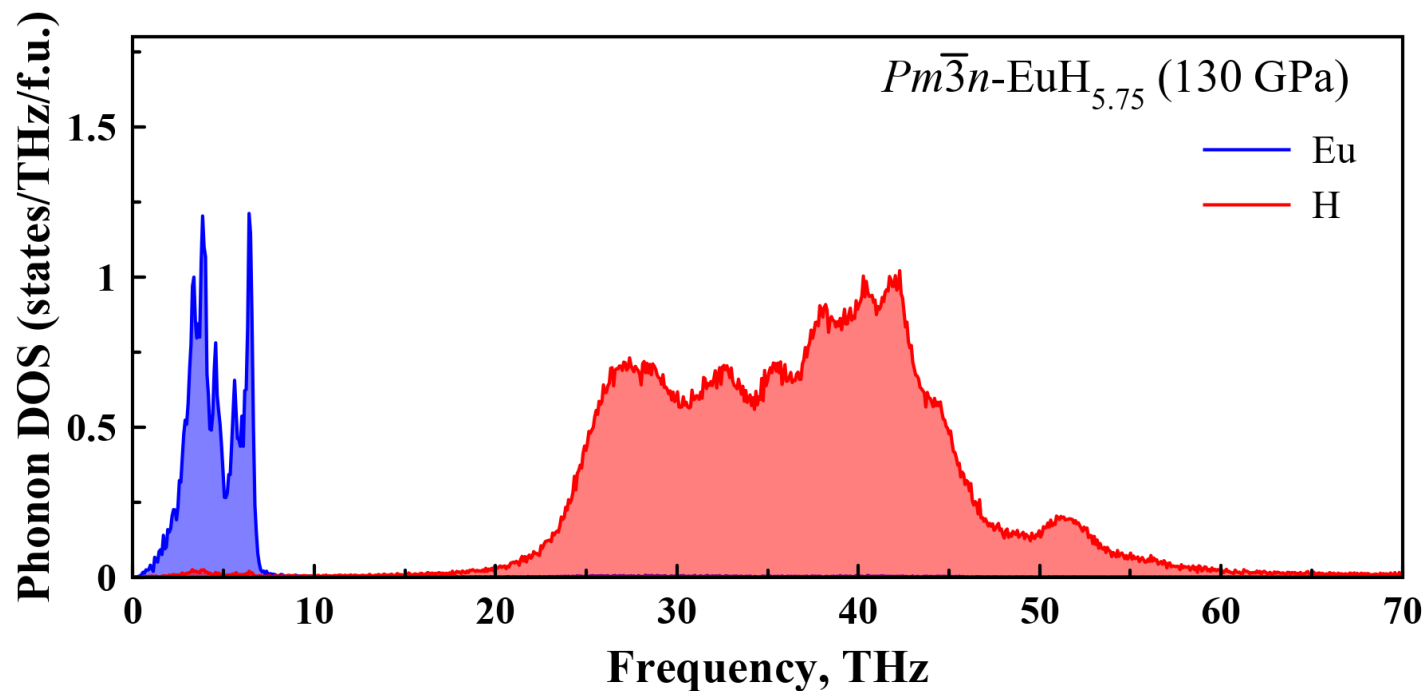


Figure S31. Anharmonic phonon density of states of  $Pm\bar{3}n$ -Eu<sub>8</sub>H<sub>46</sub> at 130 GPa and 300 K.

## Elastic Properties of the Eu–H phases

The elastic tensors of the Eu–H phases were calculated using the stress–strain relations:

$$C_{ij} = \frac{\partial \sigma_i}{\partial \eta_j} \quad (\text{S4})$$

where  $\sigma_i$  is the  $i$ th component of the stress tensor,  $\eta_j$  is the  $j$ th component of the strain tensor.

The bulk and shear moduli  $B$  and  $G$  and Young's modulus  $E$  were calculated in GPa via the Voigt–Reuss–Hill averaging.<sup>35,36</sup> Using the obtained values of the elastic moduli, we calculated the velocities of longitudinal and transverse acoustic waves:

$$v_{\text{LA}} = \sqrt{\frac{C_{11}}{\rho}}, \quad v_{\text{TA}} = \sqrt{\frac{C_{11} - C_{12}}{2\rho}} \quad (\text{S5})$$

where  $C_{11}$ ,  $C_{12}$  are the elastic constants,  $\rho$  is the density of a compound. The obtained values allow us to estimate the Debye temperature:<sup>36</sup>

$$\vartheta_D = \frac{h}{k_B} \left[ \frac{3n}{4\pi} \left( \frac{N_A \cdot \rho}{M} \right) \right]^{\frac{1}{3}} v_m \quad (\text{S6})$$

where  $h$ ,  $k_B$ ,  $N_A$  are the Planck, Boltzmann, and Avogadro constants, and  $v_m$  is the average velocity of acoustic waves calculated with the following formula:

$$v_m = \left[ \frac{1}{3} \left( \frac{2}{v_{\text{TA}}^3} + \frac{1}{v_{\text{LA}}^3} \right) \right]^{-1/3} \quad (\text{S7})$$

**Table S19.** Elastic and thermodynamic parameters of EuH<sub>9</sub> at 130 GPa (SOC+U). To simplify the calculations, ENCUT was reduced to 400–500 eV.

| Parameter                                | $P6_3/mmc$ -EuH <sub>9</sub> | $F\bar{4}3m$ -EuH <sub>9</sub> |
|--|------------------------------|--------------------------------|
| $a$ , Å                                  | 3.5450                       | 5.009                          |
| $c$ , Å                                  | 5.9303                       | -                              |
| $V_{\text{DFT}}$ , Å <sup>3</sup>        | 32.27                        | 31.41                          |
| $C_{11}$ , GPa                           | 466                          | 561                            |
| $C_{12}$ , GPa                           | 198                          | 112                            |
| $C_{13}$ , GPa                           | 226                          | 112                            |
| $C_{33}$ , GPa                           | 439                          | 561                            |
| $C_{44}$ , GPa                           | 143                          | 148                            |
| $B$ , GPa                                | 297                          | 261                            |
| $G$ , GPa                                | 131                          | 175                            |
| $E$ , GPa                                | 343                          | 429                            |
| Poisson's ratio $\eta$                   | 0.307                        | 0.226                          |
| Debye temperature $\theta_D$ , K         | 970                          | 987                            |
| $\omega_{\text{og}} = 0.827\theta_D$ , K | 802                          | 817                            |

## References

- (1) Somayazulu, M.; Ahart, M.; Mishra, A. K.; Geballe, Z. M.; Baldini, M.; Meng, Y.; Struzhkin, V. V.; Hemley, R. J. Evidence for Superconductivity above 260 K in Lanthanum Superhydride at Megabar Pressures. *Phys. Rev. Lett.* **2019**, *122*, 027001.
- (2) Semenok, D. V.; Kvashnin, A. G.; Ivanova, A. G.; Svitlyk, V.; Fominski, V. Yu.; Sadakov, A. V.; Sobolevskiy, O. A.; Pudalov, V. M.; Troyan, I. A.; Oganov, A. R. Superconductivity at 161 K in Thorium Hydride ThH10: Synthesis and Properties. *Mater. Today* **2020**, *33*, 36–44.
- (3) Zhou, D.; Semenok, D. V.; Duan, D.; Xie, H.; Chen, W.; Huang, X.; Li, X.; Liu, B.; Oganov, A. R.; Cui, T. Superconducting Praseodymium Superhydrides. *Sci. Adv.* **2020**, *6*, eaax6849.
- (4) Zhou, D.; Semenok, D. V.; Xie, H.; Huang, X.; Duan, D.; Aperis, A.; Oppeneer, P. M.; Galasso, M.; Kartsev, A. I.; Kvashnin, A. G., et al. High-Pressure Synthesis of Magnetic Neodymium Polyhydrides. *J. Am. Chem. Soc.* **2020**, *142*, 2803–2811.
- (5) Nylén, J.; Sato, T.; Soignard, E.; Yarger, J. L.; Stoyanov, E.; Häussermann, U. Thermal Decomposition of Ammonia Borane at High Pressures. *J. Chem. Phys.* **2009**, *131*, 104506.
- (6) Baitalow, F.; Wolf, G.; Grolier, J.-P. E.; Dan, F.; Randzio, S. L. Thermal Decomposition of Ammonia-Borane under Pressures up to 600bar. *Thermochim. Acta* **2006**, *445*, 121–125.
- (7) Eremets, M. I. Megabar High-Pressure Cells for Raman Measurements. *J. Raman Spectrosc.* **2003**, *34*, 515–518.
- (8) Zhang, L.-L.; Yan, S.; Jiang, S.; Yang, K.; Wang, H.; He, S.-M.; Liang, D.-X.; Zhang, L.; He, Y.; Lan, X.-Y.; Hard X-ray micro-focusing beamline at SSRF. *Nucl. Sci. Tech.* **2015**, *26*, 60101–60101.
- (9) Ohishi, Y.; Hirao, N.; Sata, N.; Hirose, K.; Takata, M. Highly Intense Monochromatic X-Ray Diffraction Facility for High-Pressure Research at SPring-8. *High Press. Res.* **2008**, *28*, 163–173.
- (10) Prescher, C.; Prakapenka, V. B. DIOPTAS: A Program for Reduction of Two-Dimensional X-Ray Diffraction Data and Data Exploration. *High Press. Res.* **2015**, *35*, 223–230.
- (11) Petříček, V.; Dušek, M.; Palatinus, L. Crystallographic Computing System JANA2006: General Features. *Z. Für Krist. - Cryst. Mater.* **2014**, *229*, 345–352.
- (12) Le Bail, A.; Duroy, H.; Fourquet, J. L. Ab-Initio Structure Determination of LiSbWO<sub>6</sub> by X-Ray Powder Diffraction. *Mater. Res. Bull.* **1988**, *23*, 447–452.
- (13) Kresse, G.; Furthmüller, J. Efficient Iterative Schemes for Ab Initio Total-Energy Calculations Using a Plane-Wave Basis Set. *Phys. Rev. B* **1996**, *54*, 11169–11186.
- (14) Kresse, G.; Hafner, J. Ab Initio Molecular Dynamics for Liquid Metals. *Phys. Rev. B* **1993**, *47*, 558–561.
- (15) Kresse, G.; Hafner, J. Ab Initio Molecular-Dynamics Simulation of the Liquid-Metal Amorphous-Semiconductor Transition in Germanium. *Phys. Rev. B* **1994**, *49*, 14251–14269.
- (16) Perdew, J. P.; Burke, K.; Ernzerhof, M. Generalized Gradient Approximation Made Simple. *Phys Rev Lett* **1997**, *78*, 1396–1396.
- (17) Blöchl, P. E. Projector Augmented-Wave Method. *Phys. Rev. B* **1994**, *50*, 17953–17979.
- (18) Kresse, G.; Joubert, D. From Ultrasoft Pseudopotentials to the Projector Augmented-Wave Method. *Phys. Rev. B* **1999**, *59*, 1758–1775.
- (19) Monkhorst, H. J.; Pack, J. D. Special Points for Brillouin-Zone Integrations. *Phys Rev B* **1976**, *13*, 5188–5192.
- (20) Galeev, T. R.; Dunnington, B. D.; Schmidt, J. R.; Boldyrev, A. I. Solid State Adaptive Natural Density Partitioning: A Tool for Deciphering Multi-Center Bonding in Periodic Systems. *Phys. Chem. Chem. Phys.* **2013**, *15*, 5022–5029.
- (21) Zubarev, D. Y.; Boldyrev, A. I. Developing Paradigms of Chemical Bonding: Adaptive Natural Density Partitioning. *Phys. Chem. Chem. Phys.* **2008**, *10*, 5207–5217.
- (22) Tkachenko, N. V.; Boldyrev, A. I. Chemical Bonding Analysis of Excited States Using the Adaptive Natural Density Partitioning Method. *Phys. Chem. Chem. Phys.* **2019**, *21*, 9590–9596.
- (23) Dunnington, B. D.; Schmidt, J. R. Generalization of Natural Bond Orbital Analysis to Periodic Systems: Applications to Solids and Surfaces via Plane-Wave Density Functional Theory. *J. Chem. Theory Comput.* **2012**, *8*, 1902–1911.

- (24) Tkachenko, N. V.; Steglenko, D.; Fedik, N.; Boldyreva, N. M.; Minyaev, R. M.; Minkin, V. I.; Boldyrev, A. I. Superoctahedral Two-Dimensional Metallic Boron with Peculiar Magnetic Properties. *Phys. Chem. Chem. Phys.* **2019**, *21*, 19764–19771.
- (25) Tkachenko, N. V.; Song, B.; Steglenko, D.; Minyaev, R. M.; Yang, L.-M.; Boldyrev, A. I. Computational Prediction of the Low-Temperature Ferromagnetic Semiconducting 2D SiN Monolayer. *Phys. Status Solidi B* **2020**, *257*, 1900619.
- (26) Dong, X.; Oganov, A. R.; Goncharov, A. F.; Stavrou, E.; Lobanov, S.; Saleh, G.; Qian, G.-R.; Zhu, Q.; Gatti, C.; Deringer, V. L., et al. A Stable Compound of Helium and Sodium at High Pressure. *Nat. Chem.* **2017**, *9*, 440–445.
- (27) Zhang, H.; Li, Y.; Hou, J.; Tu, K.; Chen, Z. FeB<sub>6</sub> Monolayers: The Graphene-like Material with Hypercoordinate Transition Metal. *J. Am. Chem. Soc.* **2016**, *138*, 5644–5651.
- (28) Yang, L.-M.; Bačić, V.; Popov, I. A.; Boldyrev, A. I.; Heine, T.; Frauenheim, T.; Ganz, E. Two-Dimensional Cu<sub>2</sub>Si Monolayer with Planar Hexacoordinate Copper and Silicon Bonding. *J. Am. Chem. Soc.* **2015**, *137*, 2757–2762.
- (29) Dolg, M.; Stoll, H.; Preuss, H.; Pitzer, R. M. Relativistic and Correlation Effects for Element 105 (Hahnium, Ha): A Comparative Study of M and MO (M = Nb, Ta, Ha) Using Energy-Adjusted Ab Initio Pseudopotentials. *J. Phys. Chem.* **1993**, *97*, 5852–5859.
- (30) Weigend, F.; Ahlrichs, R. Balanced Basis Sets of Split Valence, Triple Zeta Valence and Quadruple Zeta Valence Quality for H to Rn: Design and Assessment of Accuracy. *Phys. Chem. Chem. Phys.* **2005**, *7*, 3297–3305.
- (31) Frisch, M. J.; Trucks, G. W.; Schlegel, H. B.; Scuseria, G. E.; Robb, M. A.; Cheeseman, J. R.; Scalmani, G.; Barone, V.; Petersson, G. A.; Nakatsuji, H., et al. *Gaussian 16 Revision C.01*; **2016**.
- (32) Giannozzi, P.; Baroni, S.; Bonini, N.; Calandra, M.; Car, R.; Cavazzoni, C.; Ceresoli, D.; Chiarotti, G. L.; Cococcioni, M.; Dabo, I. et al., QUANTUM ESPRESSO: a modular and open-source software project for quantum simulations of materials. *J. Phys.: Condens. Matter*, **2009**, *21*, 395502.
- (33) Baroni, S.; Gironcoli, S. d.; Corso, A. D.; Giannozzi, P., Phonons and related crystal properties from density-functional perturbation theory. *Rev. Mod. Phys.* **2001**, *73*, 515.
- (34) Hartwigsen, C.; Goedecker, S.; Hutter, J., Relativistic separable dual-space Gaussian pseudopotentials from H to Rn. *Phys. Rev. B*, **1998**, *58*.
- (35) Goedecker, S.; Teter, M.; Hutter, J., Separable dual-space Gaussian pseudopotentials. *Phys. Rev. B*, **1996**, *54*, 1703.
- (36) Allen, P. B.; Dynes, R. C., Transition temperature of strong-coupled superconductors reanalyzed. *Phys. Rev. B*, **1975**, *12*, 905.
- (37) Momma, K.; Izumi, F. VESTA 3 for Three-Dimensional Visualization of Crystal, Volumetric and Morphology Data. *J. Appl. Crystallogr.* **2011**, *44*, 1272–1276.
- (38) Liu, H.; Naumov, I. I.; Hoffmann, R.; Ashcroft, N. W.; Hemley, R. J. Potential High-T<sub>c</sub> Superconducting Lanthanum and Yttrium Hydrides at High Pressure. *Proc. Natl. Acad. Sci.* **2017**, *114*, 6990–6995.
- (39) Hart, G. L. W.; Nelson, L. J.; Forcade, R. W., Generating derivative structures at a fixed concentration. *Computational Materials Science*, **2012**, *59*, 101.
- (40) Shapeev, A. V. Moment tensor potentials: A class of systematically improvable interatomic potentials. *Multiscale Modeling & Simulation*, **2016**, *14*, 1153–1173.
- (41) Ladygin, V. V., Korotaev, P. Y., Yanilkin, A. V., & Shapeev, A. V., Lattice dynamics simulation using machine learning interatomic potentials. *Computational Materials Science*, **2020**, *172*, 109333.
- (42) Podryabinkin, E. V.; Shapeev, A. V. Active learning of linearly parametrized interatomic potentials. *Computational Materials Science*, **2017**, *140*, 171–180.
- (43) Dickey, J. M.; Paskin, A. Computer Simulation of the Lattice Dynamics of Solids, **1969**, *Phys. Rev.*, *188*, 1407.